# Assessing the rock failure return period on an unstable Alpine rock wall based on volume-frequency relationships: The Brenva Spur (3916 m a.s.l., Aosta Valley, Italy)

Li Fei, Michel Jaboyedoff, Antoine Guerin, François Noël, Davide Bertolo, Marc-Henri Derron, Patrick Thuegaz, Fabrizio Troilo, Ludovic Ravanel

Engineering Geology 323 (2023) 107239

Contents lists available at ScienceDirect

Engineering Geology

journal homepage: www.elsevier.com/locate/enggeo

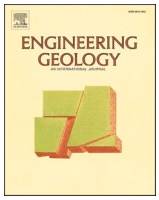

# Assessing the rock failure return period on an unstable Alpine rock wall based on volume-frequency relationships: The Brenva Spur (3916 m a.s.l., Aosta Valley, Italy)

Li Fei [a,*], Michel Jaboyedoff [a], Antoine Guerin [a,b], François Noël [a,c], Davide Bertolo [d], Marc-Henri Derron [a], Patrick Thuegaz [d], Fabrizio Troilo [e,f], Ludovic Ravanel [g]

[a] Risk Analysis Group, Institute of Earth Sciences, University of Lausanne, CH 1015 Lausanne, Switzerland
[b] Norbert SA, Engineering Geology and Hydrogeology, CH-1920 Martigny, Switzerland
[c] Geohazard and Earth Observation, Geological Survey of Norway (NGU), NO-7491 Trondheim, Norway
[d] Struttura Attività Geologiche, Regione Autonoma Valle d'Aosta, 11020 Quart, Italy
[e] Fondazione Montagna Sicura, 11013 Courmayeur (Valle d'Aosta), Italy
[f] Department of Earth and Environmental Sciences, University of Pavia, 27100 Pavia, Italy
[g] EDYTEM, Université Savoie Mont-Blanc, 73370 Le Bourget du Lac, France

ARTICLE INFO

*Keywords:*
Rockfall
Photogrammetry
SLBL
Failure scenario
Return period

ABSTRACT

Defining the relationship between volume and return period is critical when estimating the risk of rockfalls and/or rock avalanche, especially during continued global warming at high altitudes that threatens rock wall stability. Characterizing the volume-frequency relationship based on historical datasets is, however, limited by observation and quantification biases, which have not received enough attention. Here, to monitor recent activities for the Brenva Spur (Mont-Blanc massif, Italy) that is also a rock avalanche scar and estimate the return period of future rock failures based on the volume-frequency relationship (and the corresponding uncertainty), a structure-from-motion photogrammetric survey was conducted from 2017 to 2021. 39 rockfall sources with volumes ranging from 11 to 13,250 $m^3$ were identified within the scar. The total failure volume is 22,438 $m^3$, with an associated erosion rate of 15.5 mm/year, indicating very active morphodynamics possibly linked to the permafrost evolution in the spur. The volumes were characterized by a negative power-law that fits significant two events in 2016 ($3.4 \times 10^4$ $m^3$) and one in 1997 ($2.0 \times 10^6$ $m^3$) remarkably well, and the randomness of the fit was evaluated by a Monte Carlo approach. 7 potential failure scenarios ranging from $3.1 \times 10^4$ $m^3$ ($S_1$) to $4.8 \times 10^6$ $m^3$ ($S_7$) were defined according to a structural analysis and the sloping local base level concept. Their extrapolated return periods derived by the power-law fit indicate a longer return period for the maximum failure scenario than for the smaller scenarios. $S_1$ has a 50% chance of occurring every 3 years, while $S_7$ has a 50% chance of occurring every 31 years. Though the median return period of $S_7$ is 31 years, the 95% and 68.2% confidence intervals range from 8 to 399 years and 14 to 93 years, respectively, which reflects a high level of uncertainty but is realistic when considering global warming, progressive rock failure, etc. In addition to characterizing recent rock failure activities in high mountains, this study offers a preliminary examination of the return periods of some extreme scenarios and provides primary data for risk management in mountainous areas that are very sensitive to global warming.

## 1. Introduction

Rockfalls and rock avalanches are pervasive hazards in Alpine areas and can cause severe damage to infrastructure, such as ski-lifts, transportation corridors and construction located in the propagation path of such processes (Duvillard et al., 2019). Since the late 1990s, many events have been reported in Alpine regions around the world (Coe et al., 2018; Cox and Allen, 2009; Evans and Clague, 1994; Huggel, 2009; Noetzli et al., 2003; Ravanel et al., 2017; Ravanel and Deline, 2010; Sepúlveda et al., 2021). Among several preliminary and

* Corresponding author.
*E-mail address:* li.fei@unil.ch (L. Fei).

https://doi.org/10.1016/j.enggeo.2023.107239
Received 12 December 2022; Received in revised form 25 May 2023; Accepted 3 July 2023
Available online 4 July 2023

predisposing factors, the warming/degradation of permafrost is increasingly emphasized and is assumed to play a fundamental role in rock slope failures (Draebing et al., 2017; Gruber and Haeberli, 2007; Legay et al., 2021), this is especially the case during continued global warming, as has been demonstrated for example during the high temperature summers of 2003 (Gruber et al., 2004) and 2015 (Ravanel et al., 2017). Thus, with continuous climate warming driving extensive permafrost degradation, associated geologic hazards are likely to increase in Alpine regions. Although larger rock-avalanches are less frequent than rockfalls, larger events have a more significant impact on the evolution of Alpine terrain and pose a more significant threat to humans and infrastructures when they occur. Therefore, hazard analysis of rockfall/rock avalanche activity is very important not only for predictive purposes but also for conservation and mitigation efforts (Bründl et al., 2009).

Magnitude-frequency relationships are the foundation of probabilistic hazard analysis, especially concerning hazard risk estimation (De Biagi et al., 2017). The hazards (rockfalls/landslides) occurring could be derived by magnitude-frequency relationships based on the empirical data. Different data sources have been used to establish these relationships for cases with various geometries and scales. These include mapping large rockslides of different ages through satellite imagery, aerial photographs, and field surveys conducted at a specific time (Coe et al., 2018; Viani et al., 2020), considering triggering events like rainstorms or earthquakes (Malamud et al., 2004). Continuous inventories obtained by terrestrial laser scanning (TLS) (Guerin et al., 2020; Ravanel et al., 2017) and unmanned aerial vehicles (UAV) photogrammetry (Westoby et al., 2012) monitoring with different temporal interval have also been used. Ravanel and Deline (2013) implemented an observation system in the Alpine mountains specifically designed to record instances of rock failure. The magnitude-frequency relations of landslides (Brunetti et al., 2009; Dussauge et al., 2002, 2003; Malamud et al., 2004; Stark and Hovius, 2001) (related to surface area or volume) or rockfalls (Guzzetti et al., 2003; Hantz et al., 2003; Hungr et al., 1999; Larsen et al., 2010; Santana et al., 2012) (related to volume) is found often sufficiently depicted by power-law distribution over a limited range, which means that smaller landslides occur more frequently than larger ones. This distribution can be influenced by various factors, including geological context, triggering events such as rainfall or earthquakes, and local environmental conditions, resulting in a various scaling parameter (b) of fitted power laws between 0.4 and 0.9 for rock slope instability (Corominas et al., 2018). The magnitude (volume)-frequency relationship was found to be similar for different types of rock failure (Corominas et al., 2018; Dussauge et al., 2002; Guzzetti et al., 2003; Hungr et al., 1999), which indicates the potential of using the same power law observed for smaller events to extrapolate return periods for potentially larger events if the provided small events record is complete. The uncertainty and range of validity of such extrapolation are questioned and high probably affected by the largest magnitude of historical landslides that is uncommon or often missing (i.e., rockfalls and rock avalanches) (Budetta et al., 2016; Copons and Vilaplana, 2008; Graber and Santi, 2022; Guzzetti et al., 2004). Nevertheless, it is inevitable that rock failure predictions based on power-law distribution are subject to substantial uncertainties. This is especially the case for epistemic uncertainties that mainly arise due to limited knowledge (i.e., the statistical uncertainty due to the small datasets) (Straub and Schubert, 2008; Ravanel et al., 2017). Bootstrap analysis (De Biagi et al., 2017) and Monte Carlo simulations (Jaboyedoff et al., 2021; Strunden et al., 2015) are usually used to evaluate the uncertainty of magnitude-frequency relationship fittings. These fast and straightforward approaches obtain the confidence bounds of the fitted distributions to evaluate the associated uncertainties. A significant population of samples could improve a robust fit.

In the context of quantitative risk assessment of rock slope instability, a comprehensive understanding of the various potential failure scenarios (referring to reasonably expected potential slope failure sources and corresponding volumes) and their corresponding frequencies or return periods (referring to the recurrence interval at which a particular event is expected to occur) assumes critical significance in the effective prediction and protection against hazards (De Biagi et al., 2017; Fell et al., 2008; Ho, 2004). Unfortunately, the research concerning the relationship between these aspects based on the power law fitting within the domain of risk assessment of rock failure is still significantly lacking. The primary factors contributing to this deficiency are the perceived low probability associated with such scenarios and the lack of standardized definitions or assessment procedures (Corominas et al., 2005, 2018). Nonetheless, it is imperative to duly consider these potential failures, irrespective of their non-occurrence in the past. This becomes especially crucial in light of the consequence of permafrost warming induced by global climate change. More than that, there have been few studies that assess the risk (i.e., the return period of the potential large failure scenarios) posed by large historical rock avalanche scar located in the high mountainous regions where the instability of rock slope is often underestimated and poorly recorded due to inaccessibility and observation difficulties (Ravanel and Deline, 2010). A more accurate and comprehensive knowledge regarding the volume-frequency relationships of potential Alpine rock failure hazards is needed, especially under the continued climate warming (Stephan Gruber and Haeberli, 2007; Hartmeyer et al., 2020b).

Herein, the southeastern flank of the Brenva Spur (3916 m a.s.l.; Mont-Blanc massif, Aosta Valley, Italy) was investigated and studied, mainly because it corresponds to the source of the 1997 rock avalanche ($2 \times 10^6$ m$^3$) that caused two deaths and led to the destruction of a large forest area (Deline, 2001; Giani et al., 2001). The rock avalanche scar was reactivated in September 2016 with a total failure volume (two events) of approximately $3.4 \times 10^4$ m$^3$, which indicated an increasing instability of the scar. This paper presents the recent rock failure activity detected within the Brenva rock avalanche scar since July 2017 by employing a structure from motion (SfM) photogrammetric survey. Coupled with a detailed structural analysis of the rock mass, the sloping local base level (SLBL) algorithm is then used to define the potential future rock instabilities of the rock avalanche scar. Finally, 7 possible failure scenarios and their assessed return period are discussed based on the power-law fit considering the uncertainties (quantified by Monte Carlo simulations) associated with the distribution of the eroded volumes (including the one in 1997 and two in 2016) and the volumes that could collapse in the future.

## 2. Study site and geologic setting

The Brenva rock avalanche scar, mainly formed by the large rock avalanche of 1997, is located at the southeastern flank of the Brenva Spur (3916 m a.s.l.; Deline, 2001). The scar is approximately 250 m wide and 300 m high (Deline, 2009) (Fig. 1d). The Brenva Spur belongs to the upper part of the Brenva glacial basin (Mont-Blanc massif, Aosta Valley, Italy) (Fig. 1b), which is a slope glacier that now only covers 4.4 km$^2$ (7.3 in the late 1990s according to Giani et al., 2001), with a maximum length of 3.6 km, and a maximum width of 1.4 km. Before the recent disconnection of its front, the terminus of the Brenva glacier reached 1415 m a.s.l., which was the lowest glacier altitude in the Italian Alps. It is now at 2400 m a.s.l. Brenva Spur is permafrost-affected as suggested by permafrost statistical distribution models at the scale of the Alps (Boeckli et al., 2012) as well as at the scale of the Mont-Blanc massif (Magnin et al., 2015). The presence of cold hanging glaciers and ice aprons near the spur and on its northern slope also attest to this presence (Ravanel et al., 2023).

From a large scale geological point of view, granite intrusions in the gneissic basement, which occurred approximately 300 My ago (Guermani and Pennacchioni, 1998), formed the Mont-Blanc massif (mainly a granitic batholith) during the Hercynian orogeny. These two intrusion units meet at the summit of Mont Blanc (Ravanel et al., 2010). Coarse grained granites characterize the central part of the Mont-Blanc massif, while medium grain granites are distributed along its edges.

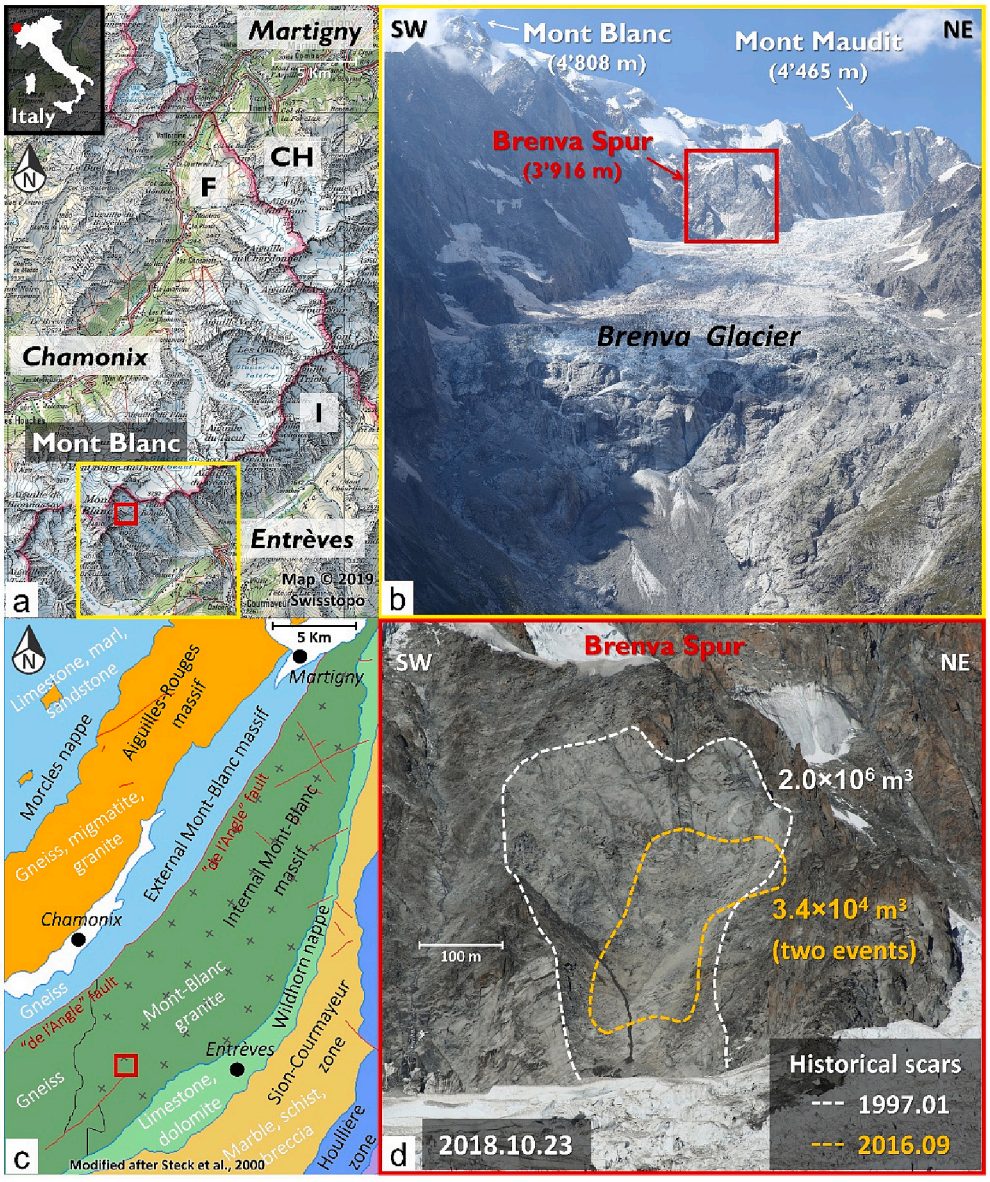


**Fig. 1.** Location and geological setting of the study area. (a) Location of the Brenva glacier basin (yellow frame) within the Mont-Blanc massif; (b) overview of the Brenva glacier basin, the red frame indicates the location of the Brenva rock avalanche scar (ph.: Joëlle Hélène Vicari, 2 September 2021); (c) simplified geotectonic map of the Mont-Blanc massif (modified after Steck et al., 2001); (d) detail view of the Brenva rock avalanche scar showing the external boundaries of the 1997 rock avalanche (white dotted line) and two large rockfall events in 2016 (orange dotted line). Elevations are in m a.s.l. (For interpretation of the references to colour in this figure legend, the reader is referred to the web version of this article.)

Additionally, the southern region is primarily made up of fine-grained granite (Guermani and Pennacchioni, 1998). More specifically, the southeastern slopes of the Mont-Blanc massif are composed of rocks originating from the Helvetic basement (Fig. 1c). These consists primarily of granites with medium or coarse biotite, sometimes porphyritic, leucocratic veins, and subvertical magmatic foliation and show weak, low grade alpine metamorphism (Steck et al., 2001).

Slopes of the Italian side around the Mont Blanc summit, including the Brenva Spur, are very steep and composed mainly of granites and massive crystalline schists. Cataclastic and mylonitic zones, with a NE–SW strike, dip steeply to the northwest and alternate with these granites. A complex system of joints and faults breaks up the slopes (Bertini et al., 1985) and form a rock mass with multiple planes and fractures consisting of highly variable directions and densities. However, the shear zones of the 1997 rock avalanche are clearly visible in the source area (Barla et al., 2000). In this Italian region, highly fractured rock masses, steep slopes, and glacier retreat have resulted in frequent rock slope failures over the centuries (Deline et al., 2015). During the 20th century, the Brenva glacial basin saw two large rock avalanches. As a result of retrogressive failures originating from the same source, five large rock masses (Deline, 2009; Deline et al., 2015) fell from the east face of the Grand Pilier d'Angle between 14 and 19 November 1920. The total volume of the failed rock ranges between 2.4 and 3.6 $\times$ $10^6$ $m^3$. On 18 January 1997, 2 $\times$ $10^6$ $m^3$ of rock detached from the Brenva Spur. In the frontal part of the avalanche, two skiers were killed at Plan Pontquet near Entrèves (1306 m a.s.l.), and the shock wave destroyed a significant portion of the forest located on the other side of the slope (Deline, 2009; Fort et al., 2009; Giani et al., 2001). The 1997 Brenva rock avalanche scar was reactivated on 22 and 30 September 2016 with two large rockslide events estimated at (1.2 $\pm$ 0.3) $\times$ $10^4$ and (1.5 $\pm$ 0.4) $\times$ $10^4$ $m^3$, respectively. The maximum total volume of the two events was estimated to be about 3.4 $\times$ $10^4$ $m^3$ (Fig. 1).

## 3. Materials and methods

### 3.1. Data acquisition

Following the reactivation of the Brenva rock avalanche scar in September 2016, SfM surveying was implemented to characterize the subsequent rock slope failure activity. Five helicopter flights performed between July 2017 and September 2021 enabled the manual acquisition of five series of high-resolution photographs of the scar using single-lens

reflex cameras. Further details of the surveys are shown in Table 1. Of the cameras used, only the Canon 7D Mark II had an integrated GPS system. However, this feature was not utilized during the data collection process. Additionally, none of the cameras were connected to any external GPS devices during the survey. Overlap between photographs varies from 60 to 80%. Due to the difficulties of access to the Brenva Spur, no ground control points (GCPs) were set during these surveys that would have been used for the generation of SfM models.

### 3.2. Data processing

#### 3.2.1. 3D points cloud model generation

All the photographs were processed with Agisoft Metashape Professional (version 1.6.2) (AMP) software (Agisoft, 2020), a dedicated photogrammetric program that uses SfM-MVS (Multi View Stereo) algorithms to generate high resolution 3D models. The main workflow followed to generate 3D point clouds by AMP includes photo pre-inspection and importation, high accuracy photo alignment, and the generation of high-quality dense point clouds (Cook and Dietze, 2019). Due to the differences in camera resolution, the number of photos and the shooting distances, the density of the final SfM point clouds over the interesting part on the Brenva rock avalanche scar is variable. As a result, the surveys conducted in July 2017, August 2017, October 2018, September 2020, and September 2021 had average point cloud densities of 83 pts./$m^2$ (0.11 m point-to-point spacing), 42 pts./$m^2$ (0.15 m point-to-point spacing), 14 pts./$m^2$ (0.27 m point-to-point spacing), 84 pts./$m^2$ (0.11 m point-to-point spacing), and 24 pts./$m^2$ (0.20 m point-to-point spacing), respectively.

#### 3.2.2. Georeferencing and registration of 3D model

These five sets of SfM points clouds were exported to CloudCompare (version 2.12. alpha) (CloudCompare, 2021) to perform further alignment and comparisons. The 3D point cloud (1 m resolution) extracted from the 2008 Digital Terrain Model (DTM) of the *Valle d'Aosta Autonomous Region* was used as the reference for the geolocation of the 3D point clouds obtained by the SfM photogrammetry surveys. Initially, rough alignment was carried out by picking at least three feature-based point pairs from the entire 3D point cloud. Then, an iterative closest point (ICP) algorithm (Besl and McKay, 1992) was applied to improve the coarse alignment by minimizing the root mean square error (RMSE) between the 3D point clouds and meshes (Abellán et al., 2010). Next, two manually selected areas were considered as stable, and the ICP was applied. The transformation matrix obtained by this process was applied to the remaining portions of the datasets that were considered as unstable. The 3D mesh was generated using the Poisson Surface Reconstruction algorithm (Kazhdan and Hoppe, 2013) and was completed in 3DReshaper software (Hexagon-Technodigit, 2016) and CloudCompare. It is worth noting that to address the absence of GCPs, the points cloud was divided into several smaller parts that were aligned independently by the ICP algorithm one by one.

#### 3.2.3. Change detection and noise filtering

The cloud-to-mesh nearest orthogonal distance (C2M distance) (Kiryati and Székely, 1993) was computed to detect surface change between two models. As a result, each point on the 3D model was assigned a scalar value corresponding to the C2M distance. Surface changes with positive and negative values are caused by an accumulation (e.g., debris, snow) or a loss (e.g., rockfall, snow melting), respectively. A visual inspection of the RGB images helps identify artefacts (shown as positive changes) along the model's edges. The raw C2M distance was denoised using a noise filter (Abellán et al., 2009) based on the nearest neighbour averaging algorithm to remove spatial noise caused by doming and spike phenomena that arise in the process of photographic 3D modelling (Guerin et al., 2017). The value from 100 neighbours was chosen for the denoising process for all the datasets in our study. Then, change detection thresholds were set to twice the standard deviations of the C2M distance for the parts supposed to be stable (Abellán et al., 2009), resulting in detection thresholds of 0.28, 0.48, 0.50, and 0.50 m for the 4 successive comparisons, respectively.

#### 3.2.4. Rockfall clustering and volume calculation

All points whose calculated C2M distance was below the threshold of detection were removed from the point cloud. The change plots and RGB photos were inspected to identify points related to rockfalls (Tonini and Abellan, 2014). Subsequently, the clusters of points associated with rockfalls were manually delineated and segmented. The rockfall volume calculation was performed using the 3D alpha-shape method following the guidelines suggested by Guerin et al. (2017) and Van Veen et al. (2017).

An example of the change calculation and rockfall sources detection method applied to the comparison between July 2017 and October 2018 that follow the above processes (Fig. 2) is shown in Fig. 3.

### 3.3. Structural analysis

Using georeferenced 3D point cloud data obtained with SfM photogrammetry and Coltop3D software (Jaboyedoff et al., 2007), we created a 3D shaded, coloured relief map that reveals topographic orientation (slope aspect and slope angle). This approach enabled us to conduct topographic structural analysis, which is crucial for studying rock mass slopes at high elevations. These areas are often remote and inaccessible, making conventional field investigations challenging. By employing this method, we detected discontinuities responsible for rock slope instabilities. On the Brenva rock avalanche scar (Fig. 4), we identified a total of seven main joint sets (rock face (RF) and J1 to J6). To gain a better understanding of how discontinuities contribute to progressive slope failure, it is essential to determine the families of discontinuities involved in past events. To achieve this, we exported the point cloud of each discontinuity family from Coltop3D and imported them into CloudCompare. Subsequently, we linked the point clouds independently with the locations of rockfall sources on the 3D model (Matasci et al., 2018). Through this method, we could determine the number of rockfalls each joint set was involved in.

### 3.4. Defining the rock instability scenarios

#### 3.4.1. Instability scenarios based on the structural analysis

In the context of steep rock slopes, the significance of main discontinuities in determining potential instability is widely acknowledged (Stead and Wolter, 2015; Wyllie and Mah, 2004). These discontinuities,

**Table 1**
Key features of the five helicopter-based SfM photogrammetry surveys.

| | Survey 1 | Survey 2 | Survey 3 | Survey 4 | Survey 5 |
|---|---|---|---|---|---|
| Date of acquisition | 4th July 2017 | 25th August 2017 | 23rd October 2018 | 18th September 2020 | 2nd September 2021 |
| Camera model | Nikon D810 | Nikon D700 | Canon EOS 7D Mark II | Canon EOS 7D Mark II | Sony ILCE 7 M2 |
| Image resolution (pixels) | 7360 × 4912 | 4256 × 2832 | 5472 × 3648 | 5472 × 3648 | 6000 × 4000 |
| Focal length (mm) | 50 | 24 | 24 | 100 | 35 |
| Number of processed images | 600 | 62 | 162 | 367 | 126 |
| Average size of images (MB) | 15 | 9.8 | 7.7 | 9.3 | 6.3 |

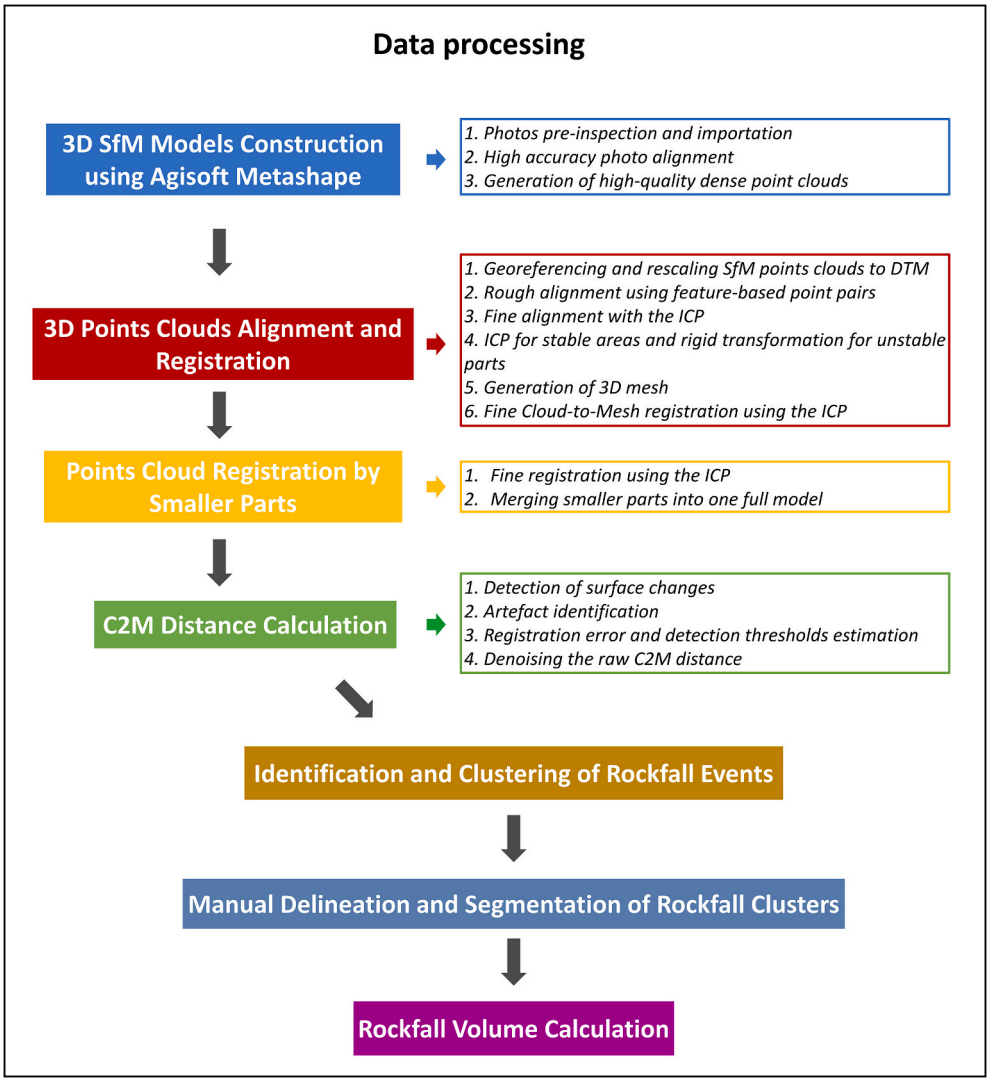


**Fig. 2.** Flowchart of the 3D points cloud processing for the rockfall detection and volume estimation.

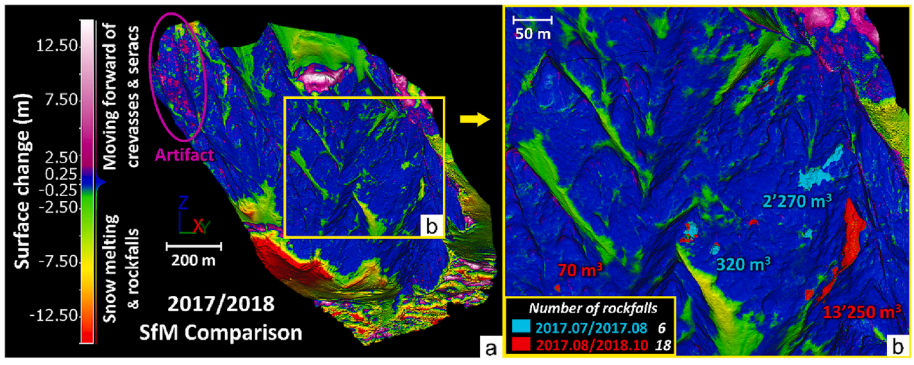


**Fig. 3.** Results of the change detection between July 2017 and October 2018. (a) Filtered point-to-mesh differences between the 2017 point cloud and the 2018 reference mesh. Positive surface changes correspond to debris and snow accumulation. Negative surface changes indicate rockfalls and snow melting. (b) Detail of the surface change and the locations of the rockfall sources (indicated in light blue and red) in Panel a. (For interpretation of the references to colour in this figure legend, the reader is referred to the web version of this article.)

which are visible at rock outcrops, can be examined by analyzing their intersecting characteristics, thereby identifying critical rock mass structures (Jaboyedoff et al., 2020). By integrating a 3D points cloud with a visual inspection of the RGB image of the scar, it becomes possible to assess the extent of potential instability scenarios, referred to as the "failure volume". This assessment mainly involves fitting planes on the exposed portions of relevant unfavourable discontinuities and analyzing the interrelationship, which aims to delineate the large kinematically unstable rock mass, between the extrapolated planes of various exposed joints. The following procedure outlines the detailed methodology employed for defining instability scenarios based on the 3D point cloud data.

1. Define at least three unfavourable discontinuities, permitting the large kinematically mobilization, based on the major historical slope

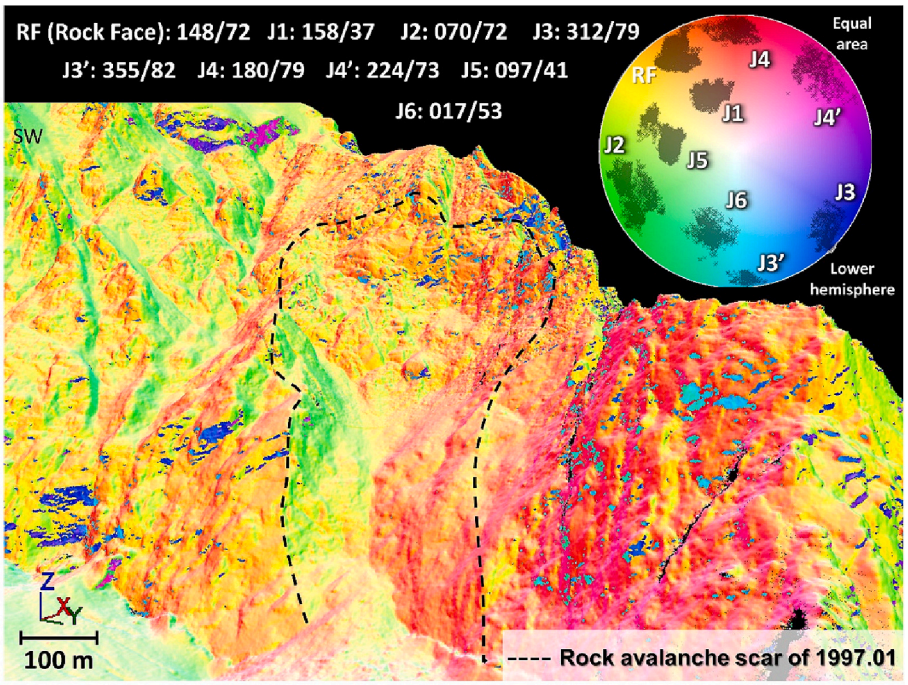


**Fig. 4.** Results of the structural analysis performed on the 2018 SfM 3D point cloud. Seven main joint sets were detected within the Brenva rock avalanche scar (spatial orientation of dip direction/dip angle is indicated by degrees). The stereographic projection displays the poles of each joint set (Schmidt stereoplot, equal area, lower hemisphere).

failure features and the spatial distribution characteristics of the main discontinuities identified in Section 3.3.

2. Extrapolate each discontinuity and fit unconstrained planes to intersect each other and delineate the contour of the instability in CloudCompare.
3. Separate out and calculate the volume delineated by the slope surface and the fitted planes.

### 3.4.2. *Instability scenarios based on the SLBL method*

The SLBL method was developed from the concept of base level in geomorphology (Jaboyedoff et al., 2019, 2020). It refers to a lower limit of the erosion process and is represented by a surface that is defined based on the altitude of streams. The SLBL method applies a similar principle to calculate the surface elevation above which the rock mass is considered susceptible to erosion. This calculation provides a potential 3D failure surface for determining the volume of instability of slopes when applied to a gridded DEM. Before calculating the failure surface, the instability's limits or perimeter must be defined using geomorphic features such as streams or morphological instability features. For example, the base of the unstable mass could be identified as either the bottom of the valley or a change in the slope angle, while the top could be defined as tension cracks or any trace of main discontinuities. The lateral boundaries could be determined by the extent of the upper geomorphic feature. Subsequently, the failure surface can be obtained using the following iterative routine (Jaboyedoff et al., 2020):

1. At each iteration $t$ (Fig. 5), for each grid node of the DEM, the SLBL method is calculating an "average" altitude $z_{temp}(t)_{i,j}$ of all the four direct neighbouring altitudes of the previous iteration $z_n(t-1)_{i,j}$, minus a positive, constant $C$(tolerance), $i,j$ represents the number of the node, i.e., for example:

$$z_{temp}(t)_{i,j} = \frac{\left(z_n(t-1)_{i,j+1} + z_n(t-1)_{i,j-1} + z_n(t-1)_{i+1,j} + z_n(t-1)_{i-1,j}\right)}{4} - C \quad (1)$$

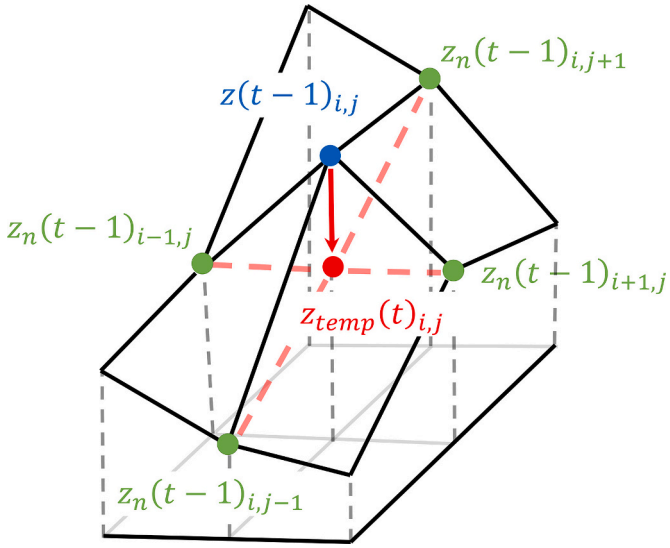


**Fig. 5.** Illustration of the SLBL iteration process (modified after Jaboyedoff et al. (2009)).

2. This process can be performed by either a simple average of a given number of neighbours or by fitting a surface. The result is a new grid which is compared to the previous one, and if $z_{temp}(t)_{i,j} < z(t-1)_{i,j}$, then $z(t)_{i,j} = z_{temp}(t)_{i,j}$; otherwise, the value is unchanged. An additional condition can be added by limiting the $z(t)_{i,j}$ value changes by another DEM or by assuming a limiting slope angle.
3. This calculation is performed iteratively and repeated until all the differences over the grid are smaller than a given threshold.

After the sliding surface is generated in 3D, the sliding volume is determined by comparing it with the original DEM.

### 3.5. Power-law and statistical analysis

It is possible to deduce the power laws that link the magnitude of a particular natural event to its frequency based on statistical analysis. For future events, these mathematical relationships can be employed to predict their type, extent, return time, and magnitude. Dussauge et al. (2003), Hungr et al. (1999), and Williams et al. (2018) found that rockfall volume and cumulative rockfall frequency have a demonstrated relationship, which can be visualized by using a complementary cumulative distribution function (CCDF) that is commonly adopted, as it avoids the ambiguities caused by the subjective selection of the bin size within the probability density function (PDF) method (Bennett et al., 2012; Strunden et al., 2015). The relationship is described by a power-law as follows (Hantz et al., 2003; Hungr et al., 1999):

$$N(V) = a\,V^{-b} \tag{2}$$

where $N$ is the cumulative number of rockfalls larger than or equal to the volume $V$ (in $m^3$) per unit of time, with $a$ and $b$ representing the preliminary factor and power-law exponent, respectively. Rockfall activity is directly connected to parameter $a$, which represents rockfall frequency, and the slope of the power-law is related to the $b$ component. Specifically, a higher value of $a$ means that more frequent rock failures occur, and a higher value of $b$ indicates that the proportion of smaller rockfall volumes is more significant than that of larger rockfall volumes. The value of $b$ can be estimated either by a least squares linear regression or the maximum likelihood estimation (MLE) approach proposed by Aki (1965):

$$b = 1/ln(10)(\langle logV > - logV_0) \tag{3}$$

Where $ln(10)$ is a constant, $< logV >$ is the average value of $logV$, and $V_0$ is the minimum volume considered (cut off volume) for the fitting, above which the power-law relationship is robust (Dussauge et al., 2002).

Assuming that the rockfall volumes follow a power-law frequency distribution, and because of the limitation of the short span of monitoring in natural environments, which would lead to epistemic uncertainties in the statistical model and prevent an exact prediction of the return period for a particular volume for a rock failure event (Straub and Schubert, 2008), we used Monte Carlo simulations to estimate the confidence intervals (uncertainties) of the return period of the potential rock failure scenarios. The simulation principle is done by simply inverting a certain sets of the power-law generating volumes, rather than removing a certain amount of sample from the large database and repeating the simulations, as suggested by Strunden et al. (2015):

$$V = \left(\frac{F_{min} + rand \times (F_{max} - F_{min})}{a}\right)^{\frac{-1}{b}} \tag{4}$$

where *rand* is a random number between 0 and 1, constant $a$ and $b$ hold same meaning as described in Eq. (2), and $F_{min}$ is the minimum frequency corresponding to the approximate time separating the 1997 event from subsequent events. $F_{max}$ is the maximum frequency corresponding to the high rockfall frequency between 2017 and 2021 in this case. In this approach, $1 \times 10^5$ datasets of rockfall inventories were simulated. It's important to emphasize again that the validity of this proposed statistical approach depends on the assumption that the rock failure volume distribution follows a power law.

## 4. Result

### 4.1. Rockfall occurrence and involved structures

Comparisons between 3D SfM point clouds allowed to identify the volumes of rock that fell from the scar, except for areas obscured by snow. As a result, the volume of the rockfall source inventory for the entire Brenva rock avalanche scar between 2017 and 2021 was established. The results showed 39 rockfall source areas, with volumes ranging from 11 to 13,250 $m^3$: 6 rockfalls occurred between July and August 2017, 18 between August 2017 and October 2018, 11 between October 2018 and September 2020, and 4 between September 2020 and September 2021 (Fig. 6). The total accumulated volume of rockfalls between 1997 and 2021 is approximately $2.05 \times 10^6$ $m^3$. In average, 9.75 events occurred per year (5600 $m^3$) during the period 2017–2021. Both the average volume (or corresponding area) and number of events each year on the Brenva rock avalanche scar has decreased in recent years (Table 2). However, the frequency of events before 2017 could be higher even though only two significant events in 2016 were listed. The rock face erosion rate was calculated by dividing the related failure volume by the scar area ($3.74 \times 10^6$ $m^2$). Table 2 reveals that the erosion rate of the rock wall was significantly higher at 44 mm/year during the period of 2017 to 2018 compared to the subsequent period of 2018 to 2021 (1.3 mm/year). The average erosion rate from 2017 to 2021 was $15.5 \pm 2.3$ mm/year. Additionally, a noticeable trend can be observed in the average depth of rockfall scars, which has progressively decreased from 1.8 m in 2017 to 0.6 m in 2021. Similarly, the average maximum scar depth has decreased from 3.7 m to 1.7 m. The largest rock failure was approximately $1.3 \times 10^4$ $m^3$ (Fig. 6). It occurred, between 2017 and 2018; the corresponding scar was first observed on the 02 September 2018. It is the only event that exceeded the magnitude of $1.0 \times 10^4$ $m^3$ during our investigation, resulting in a high erosion rate. This event was triggered on the steep ridge of the scar, where a subvertical rock face was formed by the 1997 rock avalanche and remained exposed to gravitational readjustment for 21 years. Such a large event detached from the scar is less frequent than small boulder falls. Specifically, we only documented two instances of large event in 2016 and one in 2018.

The rockfalls detected during the investigation were not clustered in specific areas, but smaller rockfalls occurred more easily in the highly fractured zone (Fig. 7) of the scar where restricted movements are expected to partly affect the upper smaller instability scenarios. Unfortunately, we could not trace the distribution of rockfall deposits, as it's challenging to determine the exact location where the rockfall has settled based on annual remote sensing surveys, especially considering the impact of melting glaciers and snow at the base. The statistical results (Fig. 8) show that the families of discontinuities RF, J1, J2, J4, and J5 are most often involved in these 39 events. Generally, the developed and persistent J1 discontinuity served as the basal plane of sliding in most detected rockfall cases. J2, J4 and J5 formed the lateral release face that constrained the volumes. The traces of the same joint sets as RF (indicated by the long purple dotted line in Fig. 7) are still extensively exposed in parallel at the top of the Brenva rock avalanche scar. The highly persistent discontinuity, RF, played a significant role as the large back release surface in the 1997 rock avalanche. Considering the importance of RF in historical large events and recent 39 boulder falls, we need to fully consider the role played by the RF discontinuity in defining potentially reasonable large rockfall scenarios in the future, which is described in Section 4.2.

### 4.2. Potential slope failure volumes

The primary progression of rock failure occurs at the intersections of major joints (Stead and Wolter, 2015). We adopted an assessment approach that incorporates both the analysis of exposed discontinuities and the SLBL concept outlined in Section 3.4 to evaluate potential failure volume scenarios. This approach led to the identification of seven rock failure scenarios, labeled as $S_1$ to $S_7$, based on their volume magnitude from smallest to largest. Among these scenarios, three were identified through geo-structural analysis, while four were derived from the SLBL concept. In the subsequent sections, we will provide a comprehensive

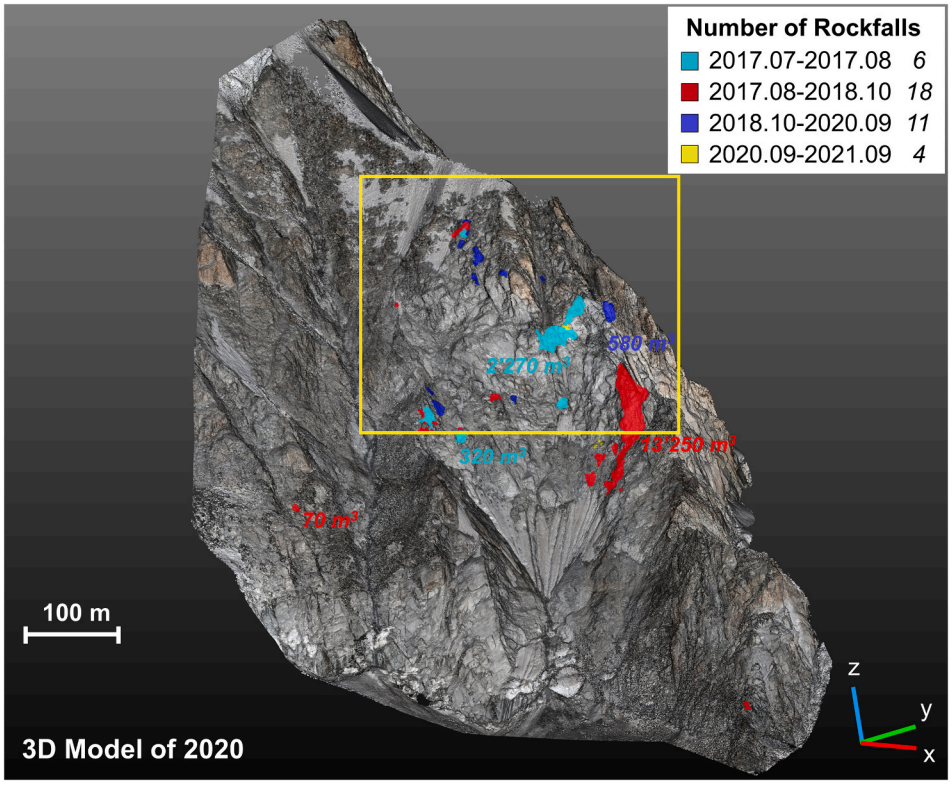


**Fig. 6.** Rock failure activity highlighted for the Brenva rock avalanche scar by employing SfM monitoring from July 2017 to September 2021. 39 rockfall sources were detected during this period. The zone demarcated by the yellow rectangle corresponds to the background photo shown in Fig. 7. (For interpretation of the references to colour in this figure legend, the reader is referred to the web version of this article.)

**Table 2**
Characteristics of the rockfalls between 2017 and 2021 in the Brenva Spur.

| Periods | Rockfalls number | Total failure volume ($m^3$) | Total failure scar area ($m^2$) | Average scar depth (m) | Average maximum scar depth (m) | Erosion rate (mm/year) |
|---|---|---|---|---|---|---|
| 07/2017 to 10/2018 | 24 | 20,576 ± 2563 | 6180 ± 214 | 1.8 ± 0.7 | 3.7 ± 0.6 | 44 ± 5.5 |
| 10/2018 to 09/2020 | 11 | 1740 ± 612 | 1225 ± 54 | 1.2 ± 0.5 | 2.5 ± 0.2 | 2.3 ± 0.8 |
| 09/2020 to 09/2021 | 4 | 121 ± 95 | 190 ± 34 | 0.6 ± 0.3 | 1.7 ± 0.2 | 0.33 ± 0.2 |

overview of the results obtained from both methods.

#### 4.2.1. Scenarios defined by structural analysis

It is worth noting that there are some assumptions in the procedure described in Section 3.4.1, such as that the scenarios defined here are supposed to represent one single detachment each and that the main joints have enough persistence under the rock mass to intersect each other. The mentioned assumptions are applicable when considering the specific case of the large rock avalanche event in 1997 that is constrained by the top tension crack developed from high persistent RF under the force of gravity, lateral limit J6, and basal plane stepped J1. Following the above approach and assumptions, we characterized three largest potential rock failures of the Brenva Spur resting on the unfavourable basal plane J1. The geometric characteristics and the volumes of three scenarios ($S_3$, $S_5$, and $S_7$) identified by such geo-structural constraints are shown in Fig. 9. The largest rock mass failure scenario ($S_7$) has a calculated volume of $4.8 \times 10^6$ $m^3$. This volume was delimited by J1 (basal sliding plane), J6 (lateral limit plane), and RF (upper limit plane), which could be an extreme and potential continuation scenario of 1997 rock avalanche. $S_7$ shows a wedge sliding failure mode plotted by Dips (Rocscience, 2022) (Fig. 10). $S_3$ is bounded by J1 (basal sliding plane), J4 (lateral limit), and J6 (lateral limit). $S_5$ are bounded by J1 (basal sliding plane), J2 (lateral limit), and J5 (bottom limit). $S_3$ and $S_5$ exhibit similar kinematically unstable characteristics as $S_7$ and could be potential sub-level continuations of the 1997 event.

#### 4.2.2. Scenarios defined by SLBL method

As mentioned in Section 3.4.2, before using the SLBL method, the limits of the potentially unstable rock mass should be defined. In this study, the structural and morphological characteristics of the Brenva spur are considered in defining the perimeter of potential instability, for instance, particular attention is given to notable features like the distinct RF trace adjacent to the scarp of the 1997 scar and the niche present on the summit. Four scenarios ($S_1$, $S_2$, $S_4$, and $S_6$) were defined based on the trace of joint set RF as the upper limit and the traces of joint sets J2, J4, and J6 as the lateral boundaries. The lower limit, referencing the base, corresponds to the slope angle break below the main scarp. Scenario $S_1$, with a calculated volume of $3.1 \times 10^4$ $m^3$, primarily encompasses the niche located at the top. $S_2$ and $S_4$ have a larger coverage area, extending southwest from $S_1$. $S_6$ expands northeastward, reaching the edge of the scar, building upon the foundation established by $S_4$. The failure volume and thickness, computed using the SLBL criteria, are illustrated in

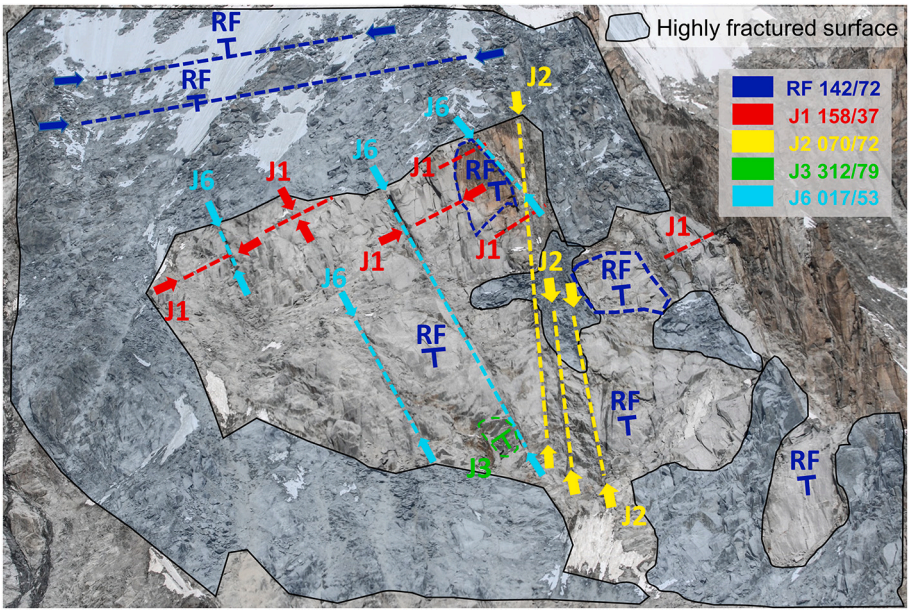


**Fig. 7.** Highly fractured scar surface located at the top of the Brenva rock avalanche scar (the background photo refers to the yellow rectangular area shown in Fig. 6). The main discontinuities, RF, JI, J2, and J6, were located on the scar and intersected with each other. Most of the small boulders fell from the highly fractured zone delineated by the closed black polyline. (For interpretation of the references to colour in this figure legend, the reader is referred to the web version of this article.)

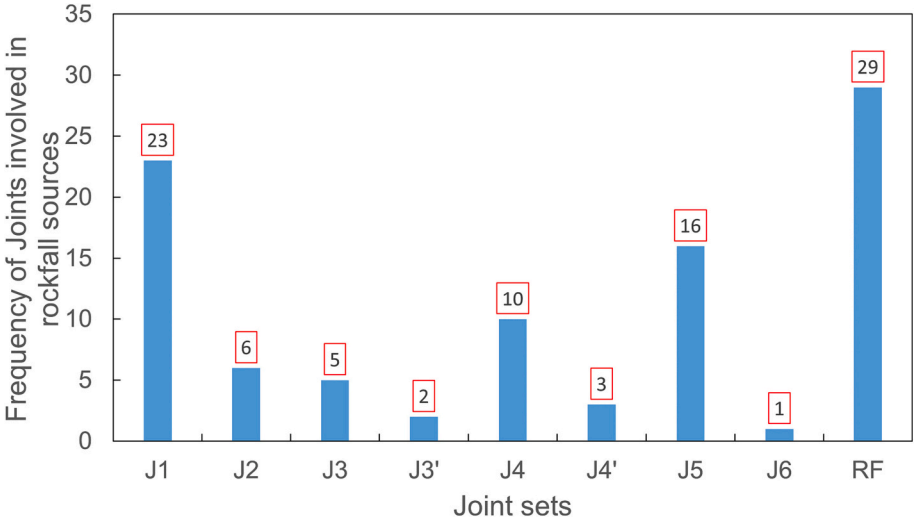


**Fig. 8.** Statistical distribution of the discontinuities involved in the 39 detected rockfall sources. The number in the red frame indicates the number of rockfalls related to the corresponding joint. RF (rock face), J1, J5, and J4 are the joint sets most involved in a rockfall in sequence. (For interpretation of the references to colour in this figure legend, the reader is referred to the web version of this article.)

Fig. 11.

We conducted a comparison between volumes computed using the SLBL method and those estimated from the structure-based analysis conducted in the previous step. The results indicate that the volumes of scenarios $S_1$, $S_2$, and $S_3$ were of similar magnitude, ranging from $3.1 \times 10^4$ $m^3$ to $8.0 \times 10^4$ $m^3$. In contrast, scenarios $S_5$ (reconstructed using structural analysis) as well as $S_4$ and $S_6$ (reconstructed using the SLBL method) exhibited higher magnitudes, ranging from $1.3 \times 10^5$ $m^3$ to $8.0 \times 10^5$ $m^3$. Comparing $S_1$ and $S_2$ with $S_3$, and $S_4$ with $S_5$, and $S_6$ with $S_7$ reveals that the volumes obtained using the structural analysis consistently exceed those obtained using the SLBL method. This can be attributed to the fact that the structural analysis-based approach does not account for interruptions caused by minor discontinuities (composite structures) or the presence of rock bridges, resulting in a simplified sliding surface and larger volume estimates. Conversely, the SLBL method creates a potential failure surface by interpolating the instability limit without considering identified structures such as J1 (bottom plane), which is assumed persistent and acts as the basal sliding plane in most instability scenarios defined by the structural approach.

### 4.3. Volume-Frequency (V-F) relationship

The method described in Section 3.5 has been used to estimate the volume-frequency (V-F) relationship for rockfalls and rock avalanches that is distributed according to a power law. Not all small events were observed and listed during the period before 2017, which may be conservative and give rock failure a calculated return period differing from its actual occurrence but agreeing with the power law. The relationship

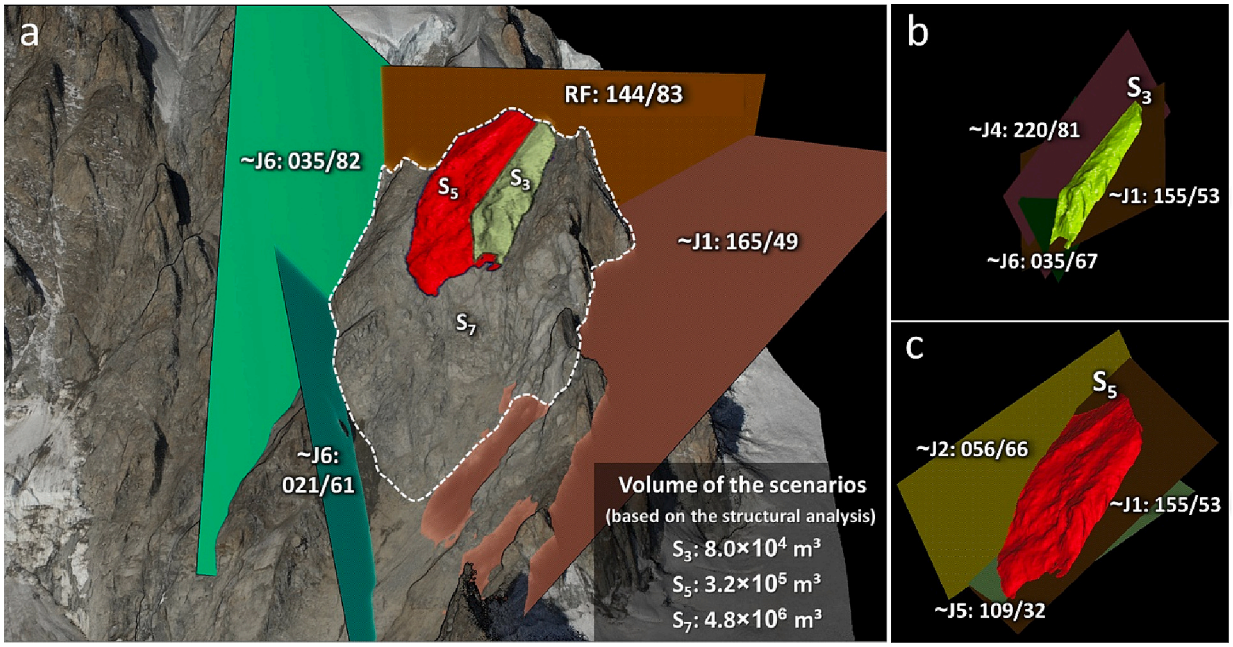


**Fig. 9.** (a) Representation of three ($S_3$, $S_5$, and $S_7$) of the seven defined large scenarios. $S_7$ controlled by discontinuity planes J1, J6, and rock face (RF), which were identified on the Brenva rock avalanche scar by the SfM model and RGB photos. (b) Plot of $S_3$ controlled by J1, J4, and J6. (c) Plot of $S_5$ controlled by J1, J2, and J5.

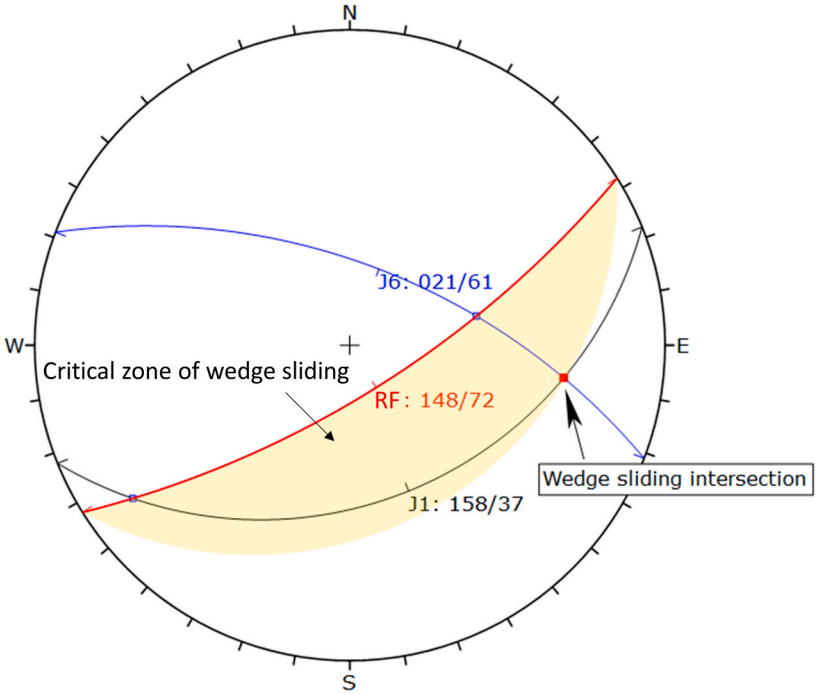


| Kinematic Analysis | Wedge Sliding | | |
|---|---|---|---|
| Slope Dip | 72 | | |
| Slope Dip Direction | 148 | | |
| Friction Angle | 30° | | |

| | Critical | Total | % |
|---|---|---|---|
| Wedge Sliding | 1 | 3 | 33.33% |

| | Color | Dip | Dip Direction | Label |
|---|---|---|---|---|
| User Planes | | | | |
| 1 | | 72 | 148 | RF: 148/72 |
| 2 | | 37 | 158 | J1: 158/37 |
| 3 | | 61 | 21 | J6: 021/61 |

| Plot Mode | Pole Vectors |
|---|---|
| Vector Count | 0 (0 Entries) |
| Intersection Mode | User Planes |
| Intersections Count | 3 |
| Hemisphere | Lower |
| Projection | Equal Angle |

**Fig. 10.** Kinematic analysis for the main joint sets involved in the defined extreme scenario $S_7$ using structural analysis. The black circular arc indicates J1, the red circular arc indicates the rock face (RF), and the blue circular arc indicates J6. The red solid rectangle indicates the intersection of J1 and J6, which is in the light orange zone (referred to as the critical zone of wedge sliding). (For interpretation of the references to colour in this figure legend, the reader is referred to the web version of this article.)

differs if we consider only the events from 2017 to 2021 or if we include two large events from 2016 and one from 1997 (Fig. 12). The corresponding power law fittings are as follows: $N(V) = 48.65\ V^{-0.58}$ and $N(V) = 33.78\ V^{-0.47}$ obtained using least square linear regression (LR). In this case, the minimum, or cut off, volume ($V_0$) of the power law fitting is set as 11.35 $m^3$. No apparent truncation or rollover and tail are observed from the distributions. The value of the latter power-law fitting exponent $b$ is equal to 0.47 and $0.43 \pm 0.14$, which was estimated using LR and MLE within the CCDF approach, respectively. Both values are in the range of an average value of $0.5 \pm 0.2$ for subvertical rock slopes and close to the value from Dussauge et al. (2002, 2003) and Hungr et al. (1999). The MLE yields a lower exponent than the LR, which indicates that larger volumes dominate the tail of the power law decay produced by MLE, or that a particular large rock failure has a shorter return period

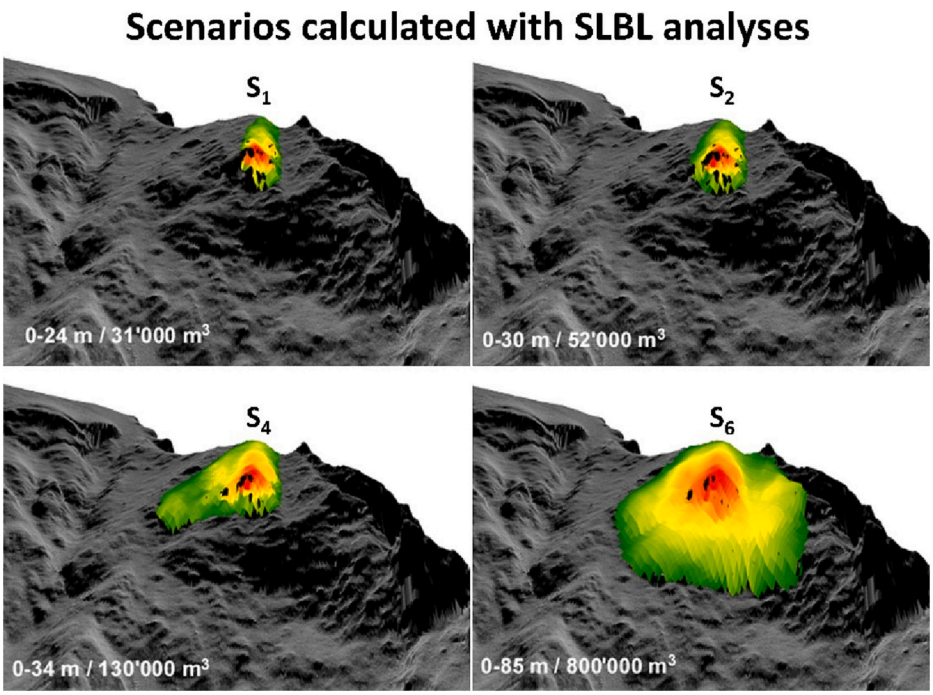


**Fig. 11.** Four ($S_1$, $S_2$, $S_4$ and $S_6$) of seven large potential failure volumes identified by the SLBL concept shown with the DEM shading of the Brenva rock avalanche scar.

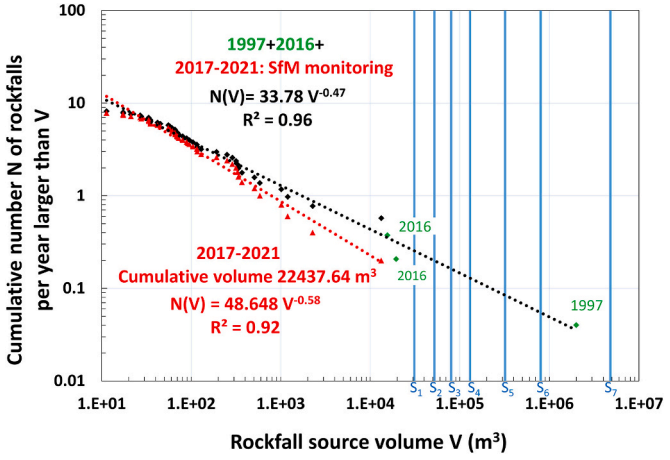


**Fig. 12.** Rockfall source volume-frequency relationship for the Brenva rock avalanche scar between 1997, 2016 and 2017–2021. Red and black data points are from SfM monitoring (2017–2021), and green data points are the 1997 and 2016 historical events. The black dashed line indicates the power law fitting for the 42 rock failures using least square regression, while the red dashed line indicates that for 39 rockfalls from 2017 to 2021. $S_1$ to $S_7$ represent seven potential rock failure scenarios defined by the combination of structural analysis and SLBL, as discussed in Section 4.2. (For interpretation of the references to colour in this figure legend, the reader is referred to the web version of this article.)

and a higher frequency by MLE, which is not supported by historical inventory.

Graber and Santi (2022) concluded that the maximum rock failure volume recorded by the historical inventory poses a more significant influence on the value of scaling exponent *b* than the minimum volume. They accomplished this by regressing these two types of volumes and by applying the scaling exponent *b* derived from published references. Undersampling large rock failure events in the fitting power-law tail profoundly affects the capacity to determine the frequency of future larger magnitude events. This also implies that the maximum rock failure magnitude in the inventory would be beneficial to constrain the unrealistic extrapolation and to obtain the accurate frequency or return period of larger failure events. These very large events are generally missing in studies on recent dynamics such as Ravanel et al. (2017). Therefore, we use the power-law fitting $N(V) = 33.78\ V^{-0.47}$ that included three large historical events as the basis for the following return period analysis and interpretation. Based on this fitting, we can preliminarily assume that an event greater than or equal to $1 \times 10^5$ m$^3$ could occur every 6.6 years, while events greater than or equal to $1 \times 10^6$ m$^3$ could occur every 20 years. Additionally, rockfalls with volumes greater than or equal to the maximum scenario ($4.8 \times 10^6$ m$^3$) would occur approximately every 41 years, though this is not observed. The frequency of events with volumes between $1 \times 10^5$ m$^3$ and $8 \times 10^5$ m$^3$ would occur every 11 years, which is close to the observed event frequency but still high for the present situation. At last, if we extrapolate the return period of the 1997 event (25 years ago) using the $N(V) = 48.65\ V^{-0.58}$ (2017 to 2021), it yields a value of 93 years that does not align with reality. This discrepancy indicates the impact of large events on the constraints of the power law distribution (referring to the *b*).

## 5. Interpretation and discussion

### 5.1. Rock failure feature and rock wall erosion

The power law distribution observed in the study fits well and does not exhibit clear truncation (Fig. 12). The absence of truncation is likely attributed to the limited observations of small events before 2017 that are yet very numerous in the Mont-Blanc massif (Ravanel and Deline, 2010, 2013). Slope failures can be divided into two types of processes based on the power-law distribution. 1) One kind of failure is the small magnitude, but very frequent, boulder falls and/or rockfalls from a highly fractured zone of granite. The stronger fitting distribution usually appears among the volumes of these types of failures. 2) Another type of failure consists of larger rock failure event that occurs with much less frequency along the intersections of the established discontinuities (Bennett et al., 2012; Katz and Aharonov, 2006). The larger the involved

rock failure volume is, the longer it takes to develop the conditions that make it prone to collapse (Abele, 1994; Bolla and Paronuzzi, 2020) also in permafrost-affected areas (Gruber and Haeberli, 2007; Hartmeyer et al., 2020a; Messenzehl and Dikau, 2017). The upper and gentler slope (48°) of the Brenva scar, characterized by highly fractured granite and exposed isolated blocks, experiences a higher frequency of small boulder detachments, with 22 rockfalls smaller than 100 $m^3$ recorded. Notably, the prominent discontinuities, such as J2, J6, and RF, as well as the north-eastern subvertical ridge (Fig. 7), greatly control the stability of the rock wall. Along these discontinuities and ridge, four rockfalls exceeding 1000 $m^3$ in size have been identified, comprising 80% of the total volume. The occurrence of these rockfalls (locate at the tail of the power law distribution) has directly contributed to the pronounced erosion rates evident on the rock wall.

During the five-year monitoring period, the average erosion rate of the rock wall was 15.5 mm/year. Specifically, between 2017 and 2018, the erosion rate reached 44 mm/year. The recent erosion rate from 2020 to 2021 has decreased significantly to 0.33 mm/year. When compared to other rock walls, this average erosion rate is much lower than the erosion rate observed at Drus (French side of Mont Blanc massif), which was 121.3 mm/year from 2005 to 2011 (Guerin et al., 2020). On the other hand, it is higher than the erosion rate at Gemsstock (2961 m a.s.l., Swiss Alps) (6.5 mm/year between 2006 and 2010) and at Tour Ronde (3792 m a.s.l., French Alps) (8.4 mm/year between 2005 and 2006) (data extracted from Hartmeyer et al. (2020a)). Furthermore, compared to the erosion rate of 10.32 mm/year on the Kitzsteinhorn (3060 m, a.s.l., Austrian Alps) north face in a cirque environment (recently deglaciated area) during 2011–2017 (Hartmeyer et al., 2020b), the erosion rate at our monitored rock wall is higher. However, it is important to note that the highest retreat rates in the proximal areas (closer to the glacier surface) of the Kitzsteinhorn (north face) reached 57.32 mm/year, surpassing the rate observed for Brenva between 2017 and 2018. From a long-term perspective, it is worth noting that erosional processes exhibit high discontinuity and temporal variability. Typically, the mean rock wall retreat rates (long term) for the reported cirques in high altitudes are below 1.0 mm/year (Hartmeyer et al., 2020b). Based on the remarkably high erosion rates described before in the high Alps since 2005, all the findings consistently indicate enhanced rock wall retreat during deglaciation, despite the inherent challenge of comparing geomorphic evidence across significantly different spatiotemporal scales.

### 5.2. Driving factors of rock failure

Due to the slope aspect and high elevation, the small rock detachments in the fractured zone on the Brenva scar are driven primarily by the initial condition of the slope, such as a well-developed fracture network coupled with mechanical weathering (probably driven by the thermally induced stress from cooling-heating cycles (Guerin et al., 2019)), frost weathering (caused by freeze–thaw cycles (Viani et al., 2020)), the seepage of rainwater and melting snow that induces hydraulic pressures in fractures (Krautblatter et al., 2013) (a snow source and water run-off can be seen on the upper slope and the left gully in the summer, as shown in Fig. 7), and cryogenic processes within the active layer of the permafrost (subsurface layer that thaws seasonally) (Legay et al., 2021).

However, outside of fundamental factors such as topography and structural features, the effects of climate change on the Brenva rock avalanche scar are also worth considering. Some recent large rockfalls in Mont-Blanc massif and the enhanced rockfall activities during the heat waves of 2003 and 2015 showed the impact that the permafrost degradation and glacier retreat caused by global warming has on rock instability (Deline, 2001; Ravanel et al., 2010, 2017; Viani et al., 2020). Gradually, permafrost thaw associated with unexpected heat waves over the past few decades/years might have contributed to the rock collapses in 2016 and 2018 since rock failure caused by such climate warming effects could occur rapidly or with a delay of only months or years (i.e., a direct response) (Gruber et al., 2004) by the deepening of the active layer and/or by the warming of the permafrost at depth. These parameters are measured since 2010 in 10-m-deep boreholes at the Aiguille du Midi (3842 m a.s.l.; (Magnin et al., 2015)), on the French side of the Mont-Blanc massif, 4.7 km north of the Brenva Spur. The southern borehole is located at 3753 m a.s.l. on a slope that is geologically and topographically very similar to the Brenva spur. In this south face, the average depth of the active layer for the years 2010, 2011, 2014 and 2015 (no data for 2012 and 2013) was 5.5 m with a maximum of 5.9 m for 2011. For 2016, 2017 and 2018, the depth of the active layer was quite homogeneous and much more important with an average of 6.9 m, i.e., 1.4 m more than for the previous years, indicating an accelerated degradation of the permafrost in those years. At a depth of 10 m, the mean annual rock temperature rose by >0.5 °C between 2010 and 2018, from −1.6 to −1.1 °C, again indicating a significant warming that might have contributed to the triggering of the main events of 2016 and 2018 at the Brenva Spur, which also can be strengthen by the rockfall scar depth decreasing from 3.7 m (2017–2018) to 1.7 m (2020-2021).

To other elements support the role of the permafrost degradation in the triggering: ice was observed at the scar after the event (see e.g. Cremonese et al., 2011), and the timing of the event (end of September) corresponding roughly to the period during which the depth of the active layer is maximum at the Aiguille du Midi. In addition, it can be assumed that the ridge that collapsed in 2018 seemingly experienced a faster and deeper thaw than other areas on the scar due to its sharp topography (Noetzli et al., 2003), especially after experiencing two summer heatwaves in 2003 and 2015 in the Mont-Blanc massif. Despite the lack of direct evidence for individual cases of rock slope instability and the lack of timing information on rockfalls, along with temperature and rainfall data, the impact of warming permafrost on rock failure cannot be ruled out for the Brenva rock avalanche scar. In such a remote environment it is almost impossible to have a permanent survey of the topography like the study by Williams et al. (2018). As the temperature rises rapidly in higher mountains (Gobiet et al., 2014), the magnitude and frequency of rock failure would exhibit uncertainty and likely occur at rates beyond the historical range in the future. Overall, the knowledge gained from rockfall activities in high mountains caused by permafrost degradation confirms the necessity of conducting continuously updated risk assessments for potential extreme rock instability scenarios on the 1997 Brenva rock avalanche scar.

### 5.3. Extrapolated return period of potential scenarios and uncertainty

Return period estimation is important in rockfall hazard assessment because it provides valuable information about the frequency at which rockfall events of a certain magnitude are expected to occur in a given area. It helps in understanding the long-term behavior and likelihood of future rockfall events, which is crucial for effective rockfall or rock avalanche hazard mitigation and management. We use the power law distribution calculated in the Section 4.3 (see the slanted red solid line in Fig. 13a) to extrapolate the return period of those defined 7 scenarios and use the Monte Carlo simulation to estimate the corresponding statistical uncertainties. Applying Eq. (4) for the $1.0 \times 10^5$ simulations of the distribution and assuming values for the minimum frequency, $F_{min} = 1/(25 years)$, and maximum frequency, $F_{max} = 39/(5 years) = 7.8$ events per year, it emerges that events of $>1.0 \times 10^4$ $m^3$ (served as the reference scenario $S_0$) have an approximately 50% chance of occurring every 2.1 years (simulated median power law fitting is indicated by bold slanted black solid line in Fig. 13a. However, during the 5 years of observation, the rock failure events seem to have exceeded this volume ($S_0$) only once. This event has a volume of $1.3 \times 10^4$ $m^3$, it can be assumed that at least one event was larger than $1.0 \times 10^4$ $m^3$ in five years. Based on above observation and assumption, we can evaluate the power-law fitting of these data. Using the observed frequency of approximately 0.2 events per year to exceed $1.0 \times 10^4$ $m^3$, we

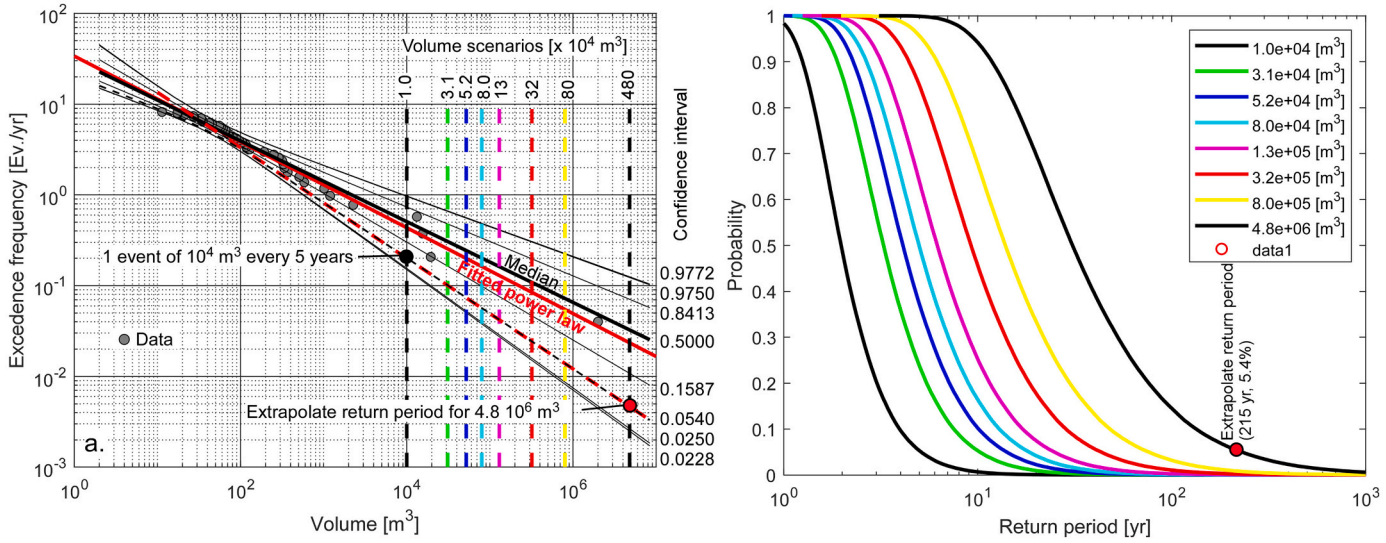


**Fig. 13.** (a) Bounds of different confidence intervals of the power-law based on Monte Carlo simulations. The dashed line indicates one of the most plausible hypotheses for the power-law. (b) Exceeding probability associated with the return period for each scenario. The black dots indicate the return period used to estimate the apparent return period based on recent past large events.

extrapolated a power-law (see the slanted red dotted line in Fig. 13a) using a second point defined by the average of $\pm\,\sigma$ (in the log) of the zone with the minimum confidence interval. This leads to an estimated return period of 215 years for the extreme event (scenario $S_7$) with a probability of 5.4%. The relationship between probability and return period for each scenario (Fig. 13b) indicates that smaller events have a shorter return period compared to larger events, assuming an equal probability of occurrence. In addition, as the magnitude of the scenarios decreased, the exceeding probability reduced while maintaining the same return period.

Upon analyzing the confidence intervals of the power law distribution obtained through Monte Carlo simulation, we observed that for $S_7$, the 95% confidence interval ranged from 8 to 399 years (a width of 391 years). Furthermore, the interval of one standard deviations for $S_7$ spanned from 14 to 93 years (a width of 79 years). The corresponding results for other scenarios are presented in Table 3. It is evident that an increase in failure volume corresponds to a wider 68% and 95% confidence interval, indicating greater variability in return period values. Thus, the uncertainty is substantial, especially for the extreme large scenarios.

The comparison between the calculated power law fitting in Section 4.3 and the simulated median power law fitting $N(V) = 30.77\ V^{-0.45}$, as depicted in Fig. 13a, clearly indicates a close resemblance. Utilizing this simulated median fitting, we estimated the median return periods for various volume scenarios, as illustrated in Fig. 14, which reveals that the median return period increases by 4 years per million cubic meters when the volume exceeds $10^6$ m$^3$. The $10^4$ m$^3$ ($10^5$ m$^3$) failure will occur every 2 years (5.5 years). It will take 15 years for a failure volume of $10^6$ m$^3$ to occur. In the case of $S_7$, the median return period, which amounts to 31 years, surpasses the duration of our inventory (25 years) by 6 years. However, it is worth noting that this additional time span is not extensive when considering the rare rock avalanche magnitude. It is important to acknowledge that our data is based on annual observations of rockfall source monitoring. Consequently, the slope of the power-law distribution may be steeper due to the possibility of multiple events occurring within a single year, as observed by Williams et al. (2018), which would result in a longer return period for those defined failure scenarios. Nevertheless, whether the large volumes were released in a single event or multiple events still remains uncertain. This ambiguity is partly accounted for within the interval of the simulated power law fitting using the Monte Carlo approach.

While caution should be exercised when extrapolating extreme volume beyond the considered volume range (De Biagi et al., 2017), it is important to highlight that all scenarios in this study, except $S_7$, remain below the largest recorded event in history occurred in 1997. These estimated return periods considering uncertainties for the six scenarios associated with the Brenva spur offer valuable references for risk assessment of rockfall/rock avalanche hazards. Anyway, improving the quality of the volume-frequency law and reducing statistical errors in the procedure can be achieved by maintaining detailed and extensive event records, along with conducting comprehensive surveys and proper definition of potential failure volumes as we did in this study.

**Table 3**
Return period and the probability of exceeding that period for the reference scenario ($S_0$:1.0 × $10^4$ m$^3$) and seven defined scenarios.

| Scenario | Volume [m$^3$] | Return periods with different exceeding probabilities (years) | | | | | | |
|---|---|---|---|---|---|---|---|---|
| | | *2.3%* | *2.5%* | *15.9%* | *50.0%* | *84.1%* | *97.5%* | *97.7%* |
| $S_0$ | 1.00E+04 | 7 | 7 | 3 | 2 | 1 | 1 | 1 |
| $S_1$ | 3.10E+04 | 14 | 14 | 6 | 3 | 2 | 2 | 2 |
| $S_2$ | 5.20E+04 | 20 | 19 | 8 | 4 | 3 | 2 | 2 |
| $S_3$ | 8.00E+04 | 27 | 25 | 10 | 5 | 3 | 2 | 2 |
| $S_4$ | 1.30E+05 | 37 | 35 | 13 | 6 | 4 | 3 | 2 |
| $S_5$ | 3.20E+05 | 66 | 63 | 22 | 9 | 5 | 3 | 3 |
| $S_6$ | 8.00E+05 | 122 | 115 | 35 | 14 | 7 | 5 | 4 |
| $S_7$ | 4.80E+06 | 399 | 375 | 93 | 31 | 14 | 8 | 8 |

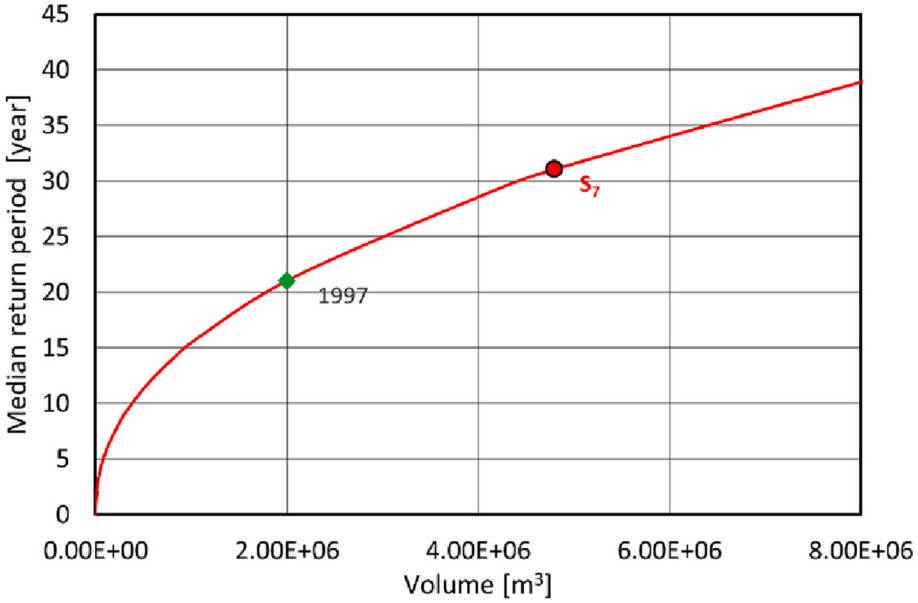


**Fig. 14.** Evolution of the median return period as a function of the rockfall volumes. The red dot indicates the median return period for $S_7$ with a volume of $4.8 \times 10^6$ $m^3$. The extrapolated median return period of 1997 rock avalanche is around 21 years indicated by the green solid diamond frame. (For interpretation of the references to colour in this figure legend, the reader is referred to the web version of this article.)

### 5.4. Issues in an overturned climatic context

Considering all of these findings and the ongoing global warming, it is highly probable that cryospheric conditions will undergo rapid changes. The current climate warming is expected to alter the occurrence of rockfalls in glacial environments over several decades following glacier downwasting (Hartmeyer et al., 2020b). Therefore, it is suggested that historical rockfall patterns in rock walls impacted by glacier retreat and permafrost degradation can only serve as reliable indicators for future events if the power law distribution is updated by the latest rock failure event accordingly. Thus, the uncertainties put forwards in our study could be real and cannot be further constrained. However, the observation made on the Drus tends to prove that rockfall activity can follow cycles after a major event (Guerin et al., 2020). For the Drus in 2005 ($0.3 \times 10^4$ $m^3$; Guerin et al., 2020) and the Brenva Spur in 1997, a rock avalanche exposed a new rock wall which, exposed to air temperatures and solar radiation, must have developed a new active layer which, in addition to mechanical readjustments linked to the main event, can trigger rockfalls. In both cases, the decay phase of disruptive activity observed today could be followed by a new phase of instability as presently suggested by the increased rockfall activities like during the very hot summer of 2022 when 282 rockfall events ($V > 100$ $m^3$) have been documented in the central part of the Mont-Blanc massif by a network of observers (Ravanel and Deline, 2013), a record since it became operational in 2007 (the previous record was for 2019 with 222 events).

Moreover, the observed decrease in rockfall activity does not mean that the entire rock avalanche scar is more stable and will be less active in the long term. The scar can be reactivated and produce a larger event (Guerin et al., 2020) as seen recently at Piz Cengalo (3678 m a.s.l.; Swiss Alps): on the 23 August 2017, around $3 \times 10^6$ $m^3$ of granitoid rock broke off from the eastern face (Mergili et al., 2020) already affected by a rock avalanche of $1.5 \times 10^6$ $m^3$ on the 27 December 2011 (Walter et al., 2020). Indeed, climate change could have a significant impact on the failure probabilities of the different scenarios. On the other hand, it is also difficult to quantify the effect of the presence of highly fractured zones (characterized by a small spacing of many families of fractures) on the gradual dismantling of the rock mass in small volumes.

## 6. Conclusions

Through five SfM photogrammetry surveys conducted in the Brenva rock avalanche scar (Aosta Valley, Italy), we identified 39 rockfall occurrences ranging from 11 to 13,250 $m^3$ between July 2017 and September 2021. This resulted in a high rock wall retreat rate of $15.5 \pm 2.3$ mm/year, possibly attributed to permafrost degradation. Monitoring data indicated a decrease in rockfall activity, with erosion rates reducing from $44 \pm 5.5$ mm/year to $0.33 \pm 0.2$ mm/year. Nevertheless, cyclical patterns in rockfall activity were observed, as exemplified by the potential activation or acceleration during heat waves in 2022 within the Mont Blanc massif.

Applying a power law-based volume-frequency relationship, we estimated the return period and corresponding uncertainties for seven potential instability volume scenarios derived from the integration of the SLBL concept and geo-structural analysis. The median return period for rock failures with volumes of $1.0 \times 10^4$ $m^3$ was estimated to be 2 years, indicating relatively frequent occurrences. However, the high confidence intervals for return periods in various scenarios introduce significant uncertainty, potentially extending the estimated return period to several decades, unless global warming initiates a new cycle of larger failures.

Considering the observed activity of small rockfalls, it is probable that the extreme scenario $S_7$ ($4.8 \times 10^6$ $m^3$) will collapse into multiple fragments due to fracking, with similar implications for other defined scenarios. Permafrost thaw and glacier retreat driven by global warming could result in shorter return periods. Nonetheless, any signs of increased activities such as boulder falls and small rockfalls should be promptly recognized as potential signals of future major rock avalanches. Regular and direct observations utilizing SfM photogrammetry or terrestrial laser scanning are essential for monitoring the evolution of the Brenva rock avalanche scar. These observations will contribute to updating the power-law fitting of rockfall sources and rockslides, thereby improving the prediction of rock slope instability scenarios regarding the return period.

## CRediT authorship contribution statement

**Li Fei:** Data curation, Investigation, Methodology, Writing – original

draft, Writing – review & editing. **Michel Jaboyedoff:** Conceptualization, Project administration, Supervision, Validation, Writing – review & editing. **Antoine Guerin:** Investigation, Methodology, Supervision. **François Noël:** Investigation. **Davide Bertolo:** Investigation, Project administration, Resources. **Marc-Henri Derron:** Methodology, Supervision. **Patrick Thuegaz:** Investigation. **Fabrizio Troilo:** Investigation. **Ludovic Ravanel:** Supervision, Validation, Writing – review & editing.

## Declaration of Competing Interest

The authors declare that they have no known competing financial interests or personal relationships that could have appeared to influence the work reported in this paper.

## Data availability

Data will be made available on request.

## References


Abele, G., 1994. Large rockslides: their causes and movement on internal sliding planes. Mt. Res. Dev. 14, 315–320. https://doi.org/10.2307/3673727.

Abellán, A., Jaboyedoff, M., Oppikofer, T., Vilaplana, J.M., 2009. Detection of millimetric deformation using a terrestrial laser scanner: experiment and application to a rockfall event. Nat. Hazards Earth Syst. Sci. https://doi.org/10.5194/nhess-9-365-2009.

Abellán, A., Calvet, J., Vilaplana, J.M., Blanchard, J., 2010. Detection and spatial prediction of rockfalls by means of terrestrial laser scanner monitoring. Geomorphology 119, 162–171. https://doi.org/10.1016/j.geomorph.2010.03.016.

Agisoft, 2020. AgiSoft Metashape Professional (Version 1.6.2 Bulid 10247) (Software). Retrieved from. http://www.agisoft.com/downloads/installer/.

Aki, K., 1965. Maximum likelihood estimate of b in the formula logN= a-bM and its confidence limits. Bull. Earthq. Res. Inst., Univ. Tokyo 43, 237–239.

Barla, G., Dutto, F., Mortara, G., 2000. Brenva glacier rock avalanche of 18 January 1997 on the Mount Blanc range, Northwest Italy. Landslide News 13, 2–5.

Bennett, G.L., Molnar, P., Eisenbeiss, H., Mcardell, B.W., 2012. Erosional power in the Swiss Alps: characterization of slope failure in the Illgraben. Earth Surf. Process. Landf. 37, 1627–1640. https://doi.org/10.1002/esp.3263.

Bertini, G., Marcucci, M., Nevini, R., Passerini, P., Sguazzoni, G., 1985. Patterns of faulting in the Mont Blanc granite. Tectonophysics 111, 65–106.

Besl, P.J., McKay, N.D., 1992. A Method for Registration of 3-D Shapes. In: IEEE Transactions on Pattern Analysis and Machine Intelligence. International Society for Optics and Photonics, pp. 239–256. https://doi.org/10.1109/34.121791.

Boeckli, L., Brenning, A., Gruber, S., Noetzli, J., 2012. Permafrost distribution in the European Alps: calculation and evaluation of an index map and summary statistics. Cryosphere 6, 807–820.

Bolla, A., Paronuzzi, P., 2020. Geomechanical Field Survey to Identify an Unstable Rock Slope: the Passo della Morte Case History (NE Italy). Rock Mech. Rock. Eng. 53, 1521–1544. https://doi.org/10.1007/s00603-019-01963-w.

Bründl, M., Romang, H.E., Bischof, N., Rheinberger, C.M., 2009. The risk concept and its application in natural hazard risk management in Switzerland. Nat. Hazards Earth Syst. Sci. 9, 801–813. https://doi.org/10.5194/nhess-9-801-2009.

Brunetti, M.T., Guzzetti, F., Rossi, M., 2009. Probability distributions of landslide volumes. Nonlinear Process. Geophys. 16, 179–188. https://doi.org/10.5194/npg-16-179-2009.

Budetta, P., De Luca, C., Nappi, M., 2016. Quantitative rockfall risk assessment for an important road by means of the rockfall risk management (RO.MA.) method. Bull. Eng. Geol. Environ. 75, 1377–1397. https://doi.org/10.1007/s10064-015-0798-6.

CloudCompare, 2021. CloudCompare (Version 2.12.alpha) [GPL Software]. Retrieved from. http://www.cloudcompare.org/.

Coe, J.A., Bessette-Kirton, E.K., Geertsema, M., 2018. Increasing rock-avalanche size and mobility in Glacier Bay National Park and Preserve, Alaska detected from 1984 to 2016 Landsat imagery. Landslides 15, 393–407. https://doi.org/10.1007/s10346-017-0879-7.

Cook, K.L., Dietze, M., 2019. Short Communication: a simple workflow for robust low-cost UAV-derived change detection without ground control points. Earth Surf. Dyn. 7, 1009–1017. https://doi.org/10.5194/esurf-7-1009-2019.

Copons, R., Vilaplana, J.M., 2008. Rockfall susceptibility zoning at a large scale: from geomorphological inventory to preliminary land use planning. Eng. Geol. 102, 142–151. https://doi.org/10.1016/j.enggeo.2008.03.020.

Corominas, J., Copons, R., Moya, J., Vilaplana, J.M., Altimir, J., Amigó, J., 2005. Quantitative assessment of the residual risk in a rockfall protected area. Landslides 2, 343–357. https://doi.org/10.1007/s10346-005-0022-z.

Corominas, J., Mavrouli, O., Ruiz-Carulla, R., 2018. Magnitude and frequency relations: are there geological constraints to the rockfall size? Landslides 15, 829–845. https://doi.org/10.1007/s10346-017-0910-z.

Cox, S.C., Allen, S.K., 2009. Vampire rock avalanches of January 2008 and 2003, Southern Alps, New Zealand. Landslides 6, 161–166. https://doi.org/10.1007/s10346-009-0149-4.

Cremonese, E., Gruber, S., Phillips, M., Pogliotti, P., Böckli, L., Noetzli, J., Suter, C., Bodin, X., Crepaz, A., Kellerer-Pirklbauer, A., 2011. Brief Communication:“ an inventory of permafrost evidence for the European Alps”. Cryosphere 5, 651–657.

De Biagi, V., Lia Napoli, M., Barbero, M., Peila, D., 2017. Estimation of the return period of rockfall blocks according to their size. Nat. Hazards Earth Syst. Sci. 17, 103–113. https://doi.org/10.5194/nhess-17-103-2017.

Deline, P., 2001. Recent Brenva rock avalanches (Valley of Aosta): new chapter in an old story? Geogr. Ann. Ser. A Phys. Geogr. 55–63.

Deline, P., 2009. Interactions between rock avalanches and glaciers in the Mont Blanc massif during the late Holocene. Quat. Sci. Rev. 28, 1070–1083. https://doi.org/10.1016/j.quascirev.2008.09.025.

Deline, P., Akçar, N., Ivy-Ochs, S., Kubik, P.W., 2015. Repeated Holocene rock avalanches onto the Brenva Glacier, Mont Blanc massif, Italy: a chronology. Quat. Sci. Rev. 126, 186–200. https://doi.org/10.1016/j.quascirev.2015.09.004.

Draebing, D., Krautblatter, M., Hoffmann, T., 2017. Thermo-cryogenic controls of fracture kinematics in permafrost rockwalls. Geophys. Res. Lett. 44, 3535–3544.

Dussauge, C., Helmstetter, A., Grasso, J.R., Hantz, D., Desvarreux, P., Jeannin, M., Giraud, A., 2002. Probabilistic approach to rock fall hazard assessment: potential of historical data analysis. Nat. Hazards Earth Syst. Sci. 2, 15–26. https://doi.org/10.5194/nhess-2-15-2002.

Dussauge, C., Grasso, J.-R., Helmstetter, A., 2003. Statistical analysis of rockfall volume distributions: implications for rockfall dynamics. J. Geophys. Res. Solid Earth 108. https://doi.org/10.1029/2001JB000650.

Duvillard, P.-A., Ravanel, L., Marcer, M., Schoeneich, P., 2019. Recent evolution of damage to infrastructure on permafrost in the French Alps. Reg. Environ. Chang. 19, 1281–1293. https://doi.org/10.1007/s10113-019-01465-z.

Evans, S.G., Clague, J.J., 1994. Recent climatic change and catastrophic geomorphic processes in mountain environments. Geomorphology 10, 107–128. https://doi.org/10.1016/0169-555X(94)90011-6.

Fell, R., Corominas, J., Bonnard, C., Cascini, L., Leroi, E., Savage, W.Z., 2008. Guidelines for landslide susceptibility, hazard and risk zoning for land-use planning. Eng. Geol. 102, 99–111. https://doi.org/10.1016/j.enggeo.2008.03.014.

Fort, M., Cossart, E., Deline, P., Dzikowski, M., Nicoud, G., Ravanel, L., Schoeneich, P., Wassmer, P., 2009. Geomorphic impacts of large and rapid mass movements: A review. In: Geomorphologie: Relief, Processus, Environnement. Groupe français de géomorphologie. https://doi.org/10.4000/geomorphologie.7495.

Giani, G.P., Silvano, S., Zanon, G., 2001. Avalanche of 18 January 1997 on Brenva glacier, Mont Blanc group, Western Italian Alps: an unusual process of formation. Ann. Glaciol. 32, 333–338. https://doi.org/10.3189/172756401781819157.

Gobiet, A., Kotlarski, S., Beniston, M., Heinrich, G., Rajczak, J., Stoffel, M., 2014. 21st century climate change in the European Alps—a review. Sci. Total Environ. 493, 1138–1151. https://doi.org/10.1016/j.scitotenv.2013.07.050.

Graber, A., Santi, P., 2022. Power law models for rockfall frequency-magnitude distributions: review and identification of factors that influence the scaling exponent. Geomorphology 418, 108463. https://doi.org/10.1016/j.geomorph.2022.108463.

Gruber, S., Haeberli, W., 2007. Permafrost in steep bedrock slopes and its temperatures-related destabilization following climate change. J. Geophys. Res. Earth Surf. 112 https://doi.org/10.1029/2006JF000547.

Gruber, S., Hoelzle, M., Haeberli, W., 2004. Permafrost thaw and destabilization of Alpine rock walls in the hot summer of 2003. Geophys. Res. Lett. 31 https://doi.org/10.1029/2004GL020051.

Guerin, A., Abellán, A., Matasci, B., Jaboyedoff, M., Derron, M.-H., Ravanel, L., 2017. Brief communication: 3-D reconstruction of a collapsed rock pillar from Web-retrieved images and terrestrial lidar data – the 2005 event of the west face of the Drus (Mont Blanc massif). Nat. Hazards Earth Syst. Sci. 17, 1207–1220. https://doi.org/10.5194/nhess-17-1207-2017.

Guerin, A., Jaboyedoff, M., Collins, B.D., Derron, M.-H., Stock, G.M., Matasci, B., Boesiger, M., Lefeuvre, C., Podladchikov, Y.Y., 2019. Detection of rock bridges by infrared thermal imaging and modeling. Sci. Rep. 9, 13138. https://doi.org/10.1038/s41598-019-49336-1.

Guerin, A., Ravanel, L., Matasci, B., Jaboyedoff, M., Deline, P., 2020. The three-stage rock failure dynamics of the Drus (Mont Blanc massif, France) since the June 2005 large event. Sci. Rep. 10, 1–20. https://doi.org/10.1038/s41598-020-74162-1.

Guermani, A., Pennacchioni, G., 1998. Brittle precursors of plastic deformation in a granite: an example from the Mont Blanc massif (Helvetic, western Alps). J. Struct. Geol. 20, 135–148. https://doi.org/10.1016/S0191-8141(97)00080-1.

Guzzetti, F., Reichenbach, P., Wieczorek, G.F., 2003. Rockfall hazard and risk assessment in the Yosemite Valley, California, USA. Nat. Hazards Earth Syst. Sci. 3, 491–503. https://doi.org/10.5194/nhess-3-491-2003.

Guzzetti, F., Reichenbach, P., Ghigi, S., 2004. Rockfall hazard and risk assessment along a transportation corridor in the Nera Valley, Central Italy. Environ. Manag. 34, 191–208. https://doi.org/10.1007/s00267-003-0021-6.

Hantz, D., Vengeon, J.M., Dussauge-Peisser, C., 2003. An historical, geomechanical and probabilistic approach to rock-fall hazard assessment. Nat. Hazards Earth Syst. Sci. 3, 693–701. https://doi.org/10.5194/nhess-3-693-2003.

Hartmeyer, I., Delleske, R., Keuschnig, M., Krautblatter, M., Lang, A., Christoph Otto, J., Schrott, L., 2020a. Current glacier recession causes significant rockfall increase: the immediate paraglacial response of deglaciating cirque walls. Earth Surf. Dyn. 8, 729–751. https://doi.org/10.5194/esurf-8-729-2020.

Hartmeyer, I., Keuschnig, M., Delleske, R., Krautblatter, M., Lang, A., Schrott, L., Prasicek, G., Otto, J.C., 2020b. A 6-year lidar survey reveals enhanced rockwall retreat and modified rockfall magnitudes/frequencies in deglaciating cirques. Earth Surf. Dyn. 8, 753–768. https://doi.org/10.5194/esurf-8-753-2020.

Hexagon-Technodigit, 2016. 3DReshaper: The 3D Scanner Software (version 11.0.7.23169). Technodigit part of Hexagon.

Ho, K., 2004. Recent advances in geotechnology for slope stabilization and landslide mitigation – Perspective from Hong Kong. In: Landslides: Evaluation and Stabilization/Glissement de Terrain: Evaluation et Stabilisation, Set of 2 Volumes, pp. 1507–1560. https://doi.org/10.1201/b16816-216.

Huggel, C., 2009. Recent extreme slope failures in glacial environments: effects of thermal perturbation. Quat. Sci. Rev. 28, 1119–1130. https://doi.org/10.1016/j.quascirev.2008.06.007.

Hungr, O., Evans, S.G., Hazzard, J., 1999. Magnitude and frequency of rock falls and rock slides along the main transportation corridors of southwestern British Columbia. Can. Geotech. J. 36, 224–238. https://doi.org/10.1139/t98-106.

Jaboyedoff, M., Metzger, R., Oppikofer, T., Couture, R., Derron, M.H., Locat, J., Turmel, D., 2007. New insight techniques to analyze rock-slope relief using DEM and 3D-imaging cloud points: COLTOP-3D software. In: Proceedings of the 1st Canada-US Rock Mechanics Symposium - Rock Mechanics Meeting Society's Challenges and Demands. OnePetro, pp. 61–68.

Jaboyedoff, M., Couture, R., Locat, P., 2009. Structural analysis of Turtle Mountain (Alberta) using digital elevation model: toward a progressive failure. Geomorphology 103, 5–16. https://doi.org/10.1016/j.geomorph.2008.04.012.

Jaboyedoff, M., Chigira, M., Arai, N., Derron, M.H., Rudaz, B., Tsou, C.Y., 2019. Testing a failure surface prediction and deposit reconstruction method for a landslide cluster that occurred during Typhoon Talas (Japan). Earth Surf. Dyn. 7, 439–458. https://doi.org/10.5194/esurf-7-439-2019.

Jaboyedoff, M., Carrea, D., Derron, M.-H., Oppikofer, T., Penna, I.M., Rudaz, B., 2020. A review of methods used to estimate initial landslide failure surface depths and volumes. Eng. Geol. 267, 105478.

Jaboyedoff, M., Choanji, T., Derron, M.H., Fei, L., Gutierrez, A., Loiotine, L., Noel, F., Sun, C., Wyser, E., Wolff, C., 2021. Introducing uncertainty in risk calculation along roads using a simple stochastic approach. Geosciences (Switzerland) 11, 143. https://doi.org/10.3390/geosciences11030143.

Katz, O., Aharonov, E., 2006. Landslides in vibrating sand box: what controls types of slope failure and frequency magnitude relations? Earth Planet. Sci. Lett. 247, 280–294. https://doi.org/10.1016/j.epsl.2006.05.009.

Kazhdan, M., Hoppe, H., 2013. Screened poisson surface reconstruction. In: ACM Transactions on Graphics. https://doi.org/10.1145/2487228.2487237.

Kiryati, N., Székely, G., 1993. Estimating shortest paths and minimal distances on digitized three-dimensional surfaces. Pattern Recogn. 26, 1623–1637. https://doi.org/10.1016/0031-3203(93)90018-R.

Krautblatter, M., Funk, D., Günzel, F.K., 2013. Why permafrost rocks become unstable: a rock–ice-mechanical model in time and space. Earth Surf. Process. Landf. 38, 876–887.

Larsen, I.J., Montgomery, D.R., Korup, O., 2010. Landslide erosion controlled by hillslope material. Nat. Geosci. 3, 247–251. https://doi.org/10.1038/ngeo776.

Legay, A., Magnin, F., Ravanel, L., 2021. Rock temperature prior to failure: Analysis of 209 rockfall events in the Mont Blanc massif (Western European Alps). Permafr. Periglac. Process. 32, 520–536.

Magnin, F., Brenning, A., Bodin, X., Deline, P., Ravanel, L., 2015. Statistical modelling of rock wall permafrost distribution: application to the Mont Blanc massif. Géomorphol. Relief Process. Environ. 20.

Malamud, B.D., Turcotte, D.L., Guzzetti, F., Reichenbach, P., 2004. Landslide inventories and their statistical properties. Earth Surf. Process. Landf. 29, 687–711. https://doi.org/10.1002/esp.1064.

Matasci, B., Stock, G.M., Jaboyedoff, M., Carrea, D., Collins, B.D., Guérin, A., Matasci, G., Ravanel, L., 2018. Assessing rockfall susceptibility in steep and overhanging slopes using three-dimensional analysis of failure mechanisms. Landslides 15, 859–878. https://doi.org/10.1007/s10346-017-0911-y.

Mergili, M., Jaboyedoff, M., Pullarello, J., Pudasaini, S.P., 2020. Back calculation of the 2017 Piz Cengalo–Bondo landslide cascade with r. avaflow: what we can do and what we can learn. Nat. Hazards Earth Syst. Sci. 20, 505–520.

Messenzehl, K., Dikau, R., 2017. Structural and thermal controls of rockfall frequency and magnitude within rockwall–talus systems (Swiss Alps). Earth Surf. Process. Landf. 42, 1963–1981. https://doi.org/10.1002/esp.4155.

Noetzli, J., Hoelzle, M., Haeberli, W., 2003. Mountain permafrost and recent Alpine rock-fall events: A GIS-based approach to determine critical factors. In: Permafrost. Swets & Zeitlinger Lisse Zürich, pp. 827–832.

Ravanel, L., Deline, P., 2010. Climate influence on rockfalls in high-Alpine steep rockwalls: The north side of the Aiguilles de Chamonix (Mont Blanc massif) since the end of the 'Little Ice Age.'. Holocene 21, 357–365. https://doi.org/10.1177/0959683610374887.

Ravanel, L., Deline, P., 2013. A network of observers in the Mont Blanc massif to study rockfalls in high alpine rockwalls. Geogr. Fis. Din. Quat. 36, 151–158.

Ravanel, L., Allignol, F., Deline, P., Gruber, S., Ravello, M., 2010. Rock falls in the Mont Blanc Massif in 2007 and 2008. Landslides 7, 493–501. https://doi.org/10.1007/s10346-010-0206-z.

Ravanel, L., Magnin, F., Deline, P., 2017. Impacts of the 2003 and 2015 summer heatwaves on permafrost-affected rock-walls in the Mont Blanc massif. Sci. Total Environ. 609, 132–143. https://doi.org/10.1016/j.scitotenv.2017.07.055.

Ravanel, L., Guillet, G., Kaushik, S., Preunkert, S., Malet, E., Magnin, F., Trouvé, E., Montagnat, M., Yan, Y., Deline, P., 2023. Ice aprons on steep high-alpine slopes: insights from the Mont-Blanc massif, Western Alps. J. Glaciol. 1–17.

Rocscience, 2022. Dips. Retrieved from. https://www.rocscience.com/software/dips.

Santana, D., Corominas, J., Mavrouli, O., Garcia-Sellés, D., 2012. Magnitude-frequency relation for rockfall scars using a Terrestrial Laser Scanner. Eng. Geol. 144–145, 50–64. https://doi.org/10.1016/j.enggeo.2012.07.001.

Sepúlveda, S.A., Alfaro, A., Lara, M., Carrasco, J., Olea-Encina, P., Rebolledo, S., Garcés, M., 2021. An active large rock slide in the Andean paraglacial environment: the Yerba Loca landslide, Central Chile. Landslides 18, 697–705. https://doi.org/10.1007/s10346-020-01564-7.

Stark, C.P., Hovius, N., 2001. The characterization of landslide size distributions. Geophys. Res. Lett. 28, 1091–1094. https://doi.org/10.1029/2000GL008527.

Stead, D., Wolter, A., 2015. A critical review of rock slope failure mechanisms: the importance of structural geology. J. Struct. Geol. https://doi.org/10.1016/j.jsg.2015.02.002.

Steck, A., Epard, J.-L., Esher, A., Gouffon, Y., Masson, H., 2001. Carte tectonique des Alpes de Suisse occidentale et des régions avoisinantes 1:100000. Office féd. Eaux Geologie (Berne) Carte géol, 73 p.

Straub, D., Schubert, M., 2008. Modeling and managing uncertainties in rock-fall hazards. Georisk 2, 1–15. https://doi.org/10.1080/17499510701835696.

Strunden, J., Ehlers, T.A., Brehm, D., Nettesheim, M., 2015. Spatial and temporal variations in rockfall determined from TLS measurements in a deglaciated valley, Switzerland. J. Geophys. Res. Earth Surf. 120, 1251–1273. https://doi.org/10.1002/2014JF003274.

Tonini, M., Abellan, A., 2014. Rockfall detection from terrestrial lidar point clouds: a clustering approach using R. J. Spat. Inform. Sci. 8, 95–110. https://doi.org/10.5311/JOSIS.2014.8.123.

Van Veen, M., Hutchinson, D.J., Kromer, R., Lato, M., Edwards, T., 2017. Effects of sampling interval on the frequency - magnitude relationship of rockfalls detected from terrestrial laser scanning using semi-automated methods. Landslides 14, 1579–1592. https://doi.org/10.1007/s10346-017-0801-3.

Viani, C., Chiarle, M., Paranunzio, R., Merlone, A., Musacchio, C., Coppa, G., Nigrelli, G., 2020. An integrated approach to investigate climate-driven rockfall occurrence in high alpine slopes: the Bessanese glacial basin, Western Italian Alps. J. Mt. Sci. 17, 2591–2610. https://doi.org/10.1007/s11629-020-6216-y.

Walter, F., Amann, F., Kos, A., Kenner, R., Phillips, M., de Preux, A., Huss, M., Tognacca, C., Clinton, J., Diehl, T., Bonanomi, Y., 2020. Direct observations of a three million cubic meter rock-slope collapse with almost immediate initiation of ensuing debris flows. Geomorphology 351, 106933. https://doi.org/10.1016/j.geomorph.2019.106933.

Westoby, M.J., Brasington, J., Glasser, N.F., Hambrey, M.J., Reynolds, J.M., 2012. "Structure-from-Motion" photogrammetry: a low-cost, effective tool for geoscience applications. Geomorphology 179, 300–314. https://doi.org/10.1016/j.geomorph.2012.08.021.

Williams, J.G., Rosser, N.J., Hardy, R.J., Brain, M.J., Afana, A.A., 2018. Optimising 4-D surface change detection: an approach for capturing rockfall magnitude-frequency. Earth Surf. Dyn. 6, 101–119. https://doi.org/10.5194/esurf-6-101-2018.

Wyllie, D.C., Mah, C., 2004. Rock Slope Engineering. CRC Press.